MOX-Report No. 36/2019

An intergrid transfer operator using radial basis functions with application to cardiac electromechanics

Salvador, M.; Dede', L.; Quarteroni, A.

MOX, Dipartimento di Matematica
Politecnico di Milano, Via Bonardi 9 - 20133 Milano (Italy)

mox-dmat@polimi.it http://mox.polimi.it

AN INTERGRID TRANSFER OPERATOR USING RADIAL BASIS FUNCTIONS WITH APPLICATION TO CARDIAC ELECTROMECHANICS

Matteo Salvador
MOX, Department of Mathematics
Politecnico di Milano
P.zza Leonardo da Vinci 32, 20133 Milan, Italy
`matteo1.salvador@polimi.it`

Luca Dede'
MOX, Department of Mathematics
Politecnico di Milano
P.zza Leonardo da Vinci 32, 20133 Milan, Italy
`luca.dede@polimi.it`

Alfio Quarteroni
MOX, Department of Mathematics
Politecnico di Milano
P.zza Leonardo da Vinci 32, 20133 Milan, Italy
Mathematics Institute, EPFL
Av. Piccard, CH-1015 Lausanne, Switzerland (Professor Emeritus)
`alfio.quarteroni@polimi.it`

ABSTRACT

In the framework of efficient partitioned numerical schemes for simulating multiphysics PDE problems, we propose using intergrid transfer operators based on radial basis functions to exchange accurately information between different PDEs defined in the same computational domain. Different (potentially non-nested) meshes can be used for the space discretization of the PDEs. The projection of the (primary) variables that are shared by the different PDEs (through the coupling terms) is carried out with Rescaled Localized Radial Basis Functions (RL-RBF). We validate our approach with a numerical test for which we also show the scalability of the intergrid transfer operator in the framework of high performance computing. Then, we apply it to the electromechanical model for the human heart function, and simulate a physiological heartbeat of an idealized left ventricle. We show that our approach enables the solution of large-scale multiphysics problems, especially when the individual models exhibit very different spatial scales.

Keywords: *intergrid operators, radial basis functions, partitioned schemes, electromechanics, heart modeling*

1 Introduction

Intergrid transfer operators between different grids defined over the same computational domain or accross different geometries are employed in a variety of applications [17], whereas radial basis functions (RBF) are used in several fields in both computer science and applied mathematics, such as neural networks [31] and mesh free methods for solving PDEs [30, 87, 88]. The application of RBF as intergrid transfer operators is documented in [29] with the aim of exchanging information on a fluid-structure interface between non-conforming meshes defined on two different computational domains. Here we aim at constructing a new appropriate intergrid transfer operator based on RBF that has the capability to interpolate in a fast and accurate way both scalar and vectorial fields between different meshes defined on the same computational domain. We deal with systems of PDEs whose solution components represent different physical variables, and we want to use non-nested grids on the same computational domain to represent these different numerical variables. For the sake of illustration we will first introduce and verify our method on a simple elliptic system with two variables u_1 and u_2 that will be approximated on two different grids. Then we will address our target application in the framework of cardiac electromechanics.

Cardiovascular diseases are indeed one of the most common causes of death globally [48] and several pathologies are still not completely understood. Mathematical modeling of the heart and numerical simulations allow a better understanding of the phenomena occurring both in physiological and pathological conditions [36, 50, 59, 83, 85]. Several types of processes occur in the human heart, such as propagation of an action potential in the myocardium, which contracts, together with the blood flowing in the four chambers (atria and ventricles) and through the valves [27, 56, 78, 79, 80]. This problem is challenging from the numerical standpoint [15, 19, 28, 42] as it involves different temporal and spatial scales. Cardiac electrophysiology, blood fluid dynamics and myocardial mechanics require a different numerical resolution in space and time, going from a really detailed one for what concerns the electric part, moving towards a bigger one for the mechanical behaviour [61, 62]. For this reason the application of multi-mesh and staggered methods is strongly justified from a physical viewpoint, and permits to solve in a really efficient way this multiphysics problem without loosing the details of the phenomena that we want to model.

In this work we focus on the electromechanical modeling of the left ventricle, which has been extensively studied over the past years [16, 21, 32], but still needs further investigations both from theoretical and numerical perspectives. For the electric part we consider the monodomain and Bueno-Orovio models [10, 58, 73]. For the mechanical part we use the Holzapfel-Ogden model [40] together with the active strain formulation [2, 3], combined with a model for the transmural heterogeneous thickening of the myocardium [7]. Myocardial fibers contraction defines the bridge between electrophysiology and mechanics [70]. From the numerical viewpoint, the Finite Element Method (FEM) is used in order to discretize in space the continuous single core models (i.e. electrophysiology, activation and mechanics) by means of piecewise linear elements, whereas time discretization is carried on using Backward Differentiation Formulas (BDFs) of order 1 [60]. As already done in literature [5, 6, 16, 36, 44], the integration of the discrete core models leads to the formulation of segregated (i.e. which are all solved separately and sequentially) and staggered (i.e. using with different timesteps) algebraic equations. The timestep changes according to the time scale of the single problem. Semi-implicit or implicit time discretizations are considered depending on the stiffness of the models. Moreover, according to the required space resolution, we use different independent (i.e. non-nested) meshes and we perform intergrid fields transfer by means of RL-RBF. We use different simplified Cauchy models to describe the blood flow inside the left ventricle. In this way we can compute how pressure and volume evolve along the heartbeat [26, 67, 85]. We also consider a prestress technique, which is applied in the pre-processing phase, to estimate the internal stresses of the myocardium at the initial time of the simulation [41, 81].

As observed before, electrophysiology and mechanics are solved separately, in a segregated fashion. We use different meshes and timesteps (staggered approach) for the two fields. After space and time discretization we solve each block linear system by means of GMRES iterations. We use our partitioned and staggered electromechanics solver to carry out a numerical simulation in the High Performance Computing framework of the whole cardiac cycle for an idealized LV geometry, and we analyze the numerical results in terms of clinically relevant indicators: specifically, we produce the so-called pressure-volume loops in order to assess the left ventricle function and its properties.

The paper is organized as follows: in Section 2 we present the interpolant based on radial basis functions that will act as intergrid transfer operator. In Section 3 we propose a test case with known exact solution to show the accuracy and the reliability of the operator introduced in Section 2. In Section 4 we apply the methodology that we have developed and tested to cardiac electromechanics, a complex framework in which different physics (electrophysiology, mechanical activation and mechanical deformation of the myocardium) and different space scales are present. We also propose a novel partitioned scheme for the time discretization of the single core models related to cardiac electromechanics, carrying out the numerical simulation of one heartbeat of an idealized left ventricle in physiological conditions. We finally draw our conclusions in Section 5.

2 Intergrid transfer operator

Our aim is to transfer the values of a certain function from one mesh to another one. However we present in this section our intergrid transfer operator in the most general framework. We exploit several properties of RBF to perform the interpolation task considering a general function f, following the idea developed in [22].

Let $f : \mathbb{R}^3 \to \mathbb{R}^d$ be a scalar ($d = 1$) or possibly vector field ($d > 1$) in the 3D setting. Given a set of M nodes $\Xi = \{\boldsymbol{\xi_m}\}_{m=1}^{M}$ in $\mathbb{R}^3$, we define an interpolant $\Pi_f(\boldsymbol{x})$ (with $\boldsymbol{x} \in \mathbb{R}^3$) of the general field f by means of radial basis functions in the following way:

$$\Pi_f(\boldsymbol{x}) = \sum_{m=1}^{M} \gamma_m^f \pi(||\boldsymbol{x} - \boldsymbol{\xi_m}||, r), \tag{1}$$

with $\{\gamma_m^f\}_{m=1}^M$ set of the interpolation weights. The radial basis function is denoted by $\pi(\cdot, r)$, which can be either globally or locally supported according to the choice of the radius r. We use Beckert & Wendland radial basis functions $\pi(||\boldsymbol{x}||, r) = \left(1 - \frac{||\boldsymbol{x}||}{r}\right)^4 \left(1 + 4\frac{||\boldsymbol{x}||}{r}\right)$, which are locally supported. Other options, involving also globally supported basis functions, are available as well [11, 25]. We introduce an interpolation matrix $\boldsymbol{\Phi}^{int} \in \mathbb{R}^{M\times M}$ such that $\boldsymbol{\Phi}^{int}_{i,j} = \pi(||\boldsymbol{\xi}_i - \boldsymbol{\xi}_j||, r)$ with $i, j = 1, ..., M$. We call $\boldsymbol{f}_\Xi$ the evaluation of the field f in all the M interpolation nodes that belong to the set Ξ. The interpolation constraint is algebraically expressed as follows:

$$\boldsymbol{\Phi}^{int}\boldsymbol{\gamma}^{\boldsymbol{f}} = \boldsymbol{f}_\Xi, \tag{2}$$

with $\boldsymbol{\gamma}^{\boldsymbol{f}} = \{\gamma_m^f\}_{m=1}^M$ solution of linear system (2).

Both fields f and $\Pi_f(\boldsymbol{x})$ have the same value at the interpolation nodes, i.e. $\Pi_f(\boldsymbol{\xi}_{\boldsymbol{m}}) = f(\boldsymbol{\xi}_{\boldsymbol{m}})$ with $m = 1, ..., M$. The choice of local radial basis functions leads to a sparse pattern of the matrix $\boldsymbol{\Phi}^{int}$. At this point, once $\Pi_f(\boldsymbol{x})$ is determined, we can evaluate the interpolant on a set $\Lambda = \{\boldsymbol{\lambda}_{\boldsymbol{n}}\}_{n=1}^N$ of N different points with respect to the interpolation nodes contained in Ξ:

$$\Pi_f(\boldsymbol{\lambda}_n) = \sum_{m=1}^{M} \gamma_m^f \pi(||\boldsymbol{\lambda}_n - \boldsymbol{\xi}_{\boldsymbol{m}}||, r). \tag{3}$$

In our application Ξ and Λ will be two different sets of nodes of two independent triangulations of the computational domain $\Omega \subset \mathbb{R}^3$ where the interpolant $\Pi_f(\cdot)$ is defined.

We introduce a matrix $\boldsymbol{\Phi}^{eval} \in \mathbb{R}^{N\times M}$ such that $\boldsymbol{\Phi}^{eval}_{i,j} = \pi(||\boldsymbol{\lambda}_i - \boldsymbol{\xi}_j||, r)$ with $i = 1, ..., N$ and $j = 1, ..., M$. This sparse matrix is used to determine $\boldsymbol{f}_\Lambda$, i.e. the evaluation of the RBF interpolant Π_f on Λ:

$$\boldsymbol{f}_\Lambda = \boldsymbol{\Phi}^{eval}\boldsymbol{\gamma}^{\boldsymbol{f}} = \boldsymbol{\Phi}^{eval}(\boldsymbol{\Phi}^{int})^{-1}\boldsymbol{f}_\Xi. \tag{4}$$

In order to obtain a smoother interpolant that is able to interpolate exactly any constant field and that is accurate for small values of the radius r [22], we rescale $\Pi_f(\boldsymbol{x})$ by the interpolant $\Pi_g(\boldsymbol{x})$ of the constant function $g(\boldsymbol{x}) = 1$, which assumes a value equal to one at each interpolation point:

$$\bar{\Pi}_f(\boldsymbol{x}) = \frac{\Pi_f(\boldsymbol{x})}{\Pi_g(\boldsymbol{x})} = \frac{\sum_{m=1}^{M} \gamma_m^f \pi(||\boldsymbol{x} - \boldsymbol{\xi}_{\boldsymbol{m}}||, r)}{\sum_{l=1}^{M} \gamma_l^g \pi(||\boldsymbol{x} - \boldsymbol{\xi}_{\boldsymbol{l}}||, r)}. \tag{5}$$

We formulate in this way Rescaled Localized Radial Basis Functions (RL-RBF).
From the algebraic perspective, the interpolation problem associated with (5) can be written in the following form:

$$\boldsymbol{\Phi}^{int}\boldsymbol{\gamma}^{\boldsymbol{f}} = \boldsymbol{f}_\Xi, \tag{6}$$

$$\boldsymbol{\Phi}^{int}\boldsymbol{\gamma}^{\boldsymbol{g}} = \boldsymbol{1}_\Xi, \tag{7}$$

where $\boldsymbol{\gamma}^{\boldsymbol{g}} = \{\gamma_m^g\}_{m=1}^M$ and $\boldsymbol{1}_\Xi$ vector of ones on the interpolation nodes defined in Ξ. Linear systems (6) and (7) are solved separately. The evaluation of interpolant $\bar{\Pi}_f$ in a specific point $\boldsymbol{x}$ is:

$$\bar{\Pi}_f(\boldsymbol{x}) = \frac{\boldsymbol{\Phi}^{eval}(\boldsymbol{\Phi}^{int})^{-1}\boldsymbol{f}_\Xi}{\boldsymbol{\Phi}^{eval}(\boldsymbol{\Phi}^{int})^{-1}\boldsymbol{1}_\Xi}, \tag{8}$$

where $(\boldsymbol{\Phi}^{eval})^T \in \mathbb{R}^M$ such that $(\boldsymbol{\Phi}^{eval})^T_j = \pi(||\boldsymbol{x} - \boldsymbol{\xi}_j||, r)$.

3 Elliptic numerical test

We want to illustrate the properties of our intergrid transfer operator in terms of scalability and convergence for both the L^2 and H^1 norms in a given domain $\Omega \subset \mathbb{R}^d$. With this aim, we propose the following test case:

$$\begin{cases} -\Delta u_1 = f_1 & \text{in } \Omega, \\ -\Delta u_2 + u_1 + \nabla u_1 \cdot \boldsymbol{v} = f_2 & \text{in } \Omega, \\ u_1 = u_2 = 0 & \text{on } \partial\Omega, \end{cases} \tag{9}$$

with $\Omega = (-1, 1)^3$ and $\boldsymbol{v} = \boldsymbol{1}$. The forcing terms are:

$$f_1 = 3\pi^2 \text{sin}(\pi x)\text{sin}(\pi y)\text{sin}(\pi z),$$

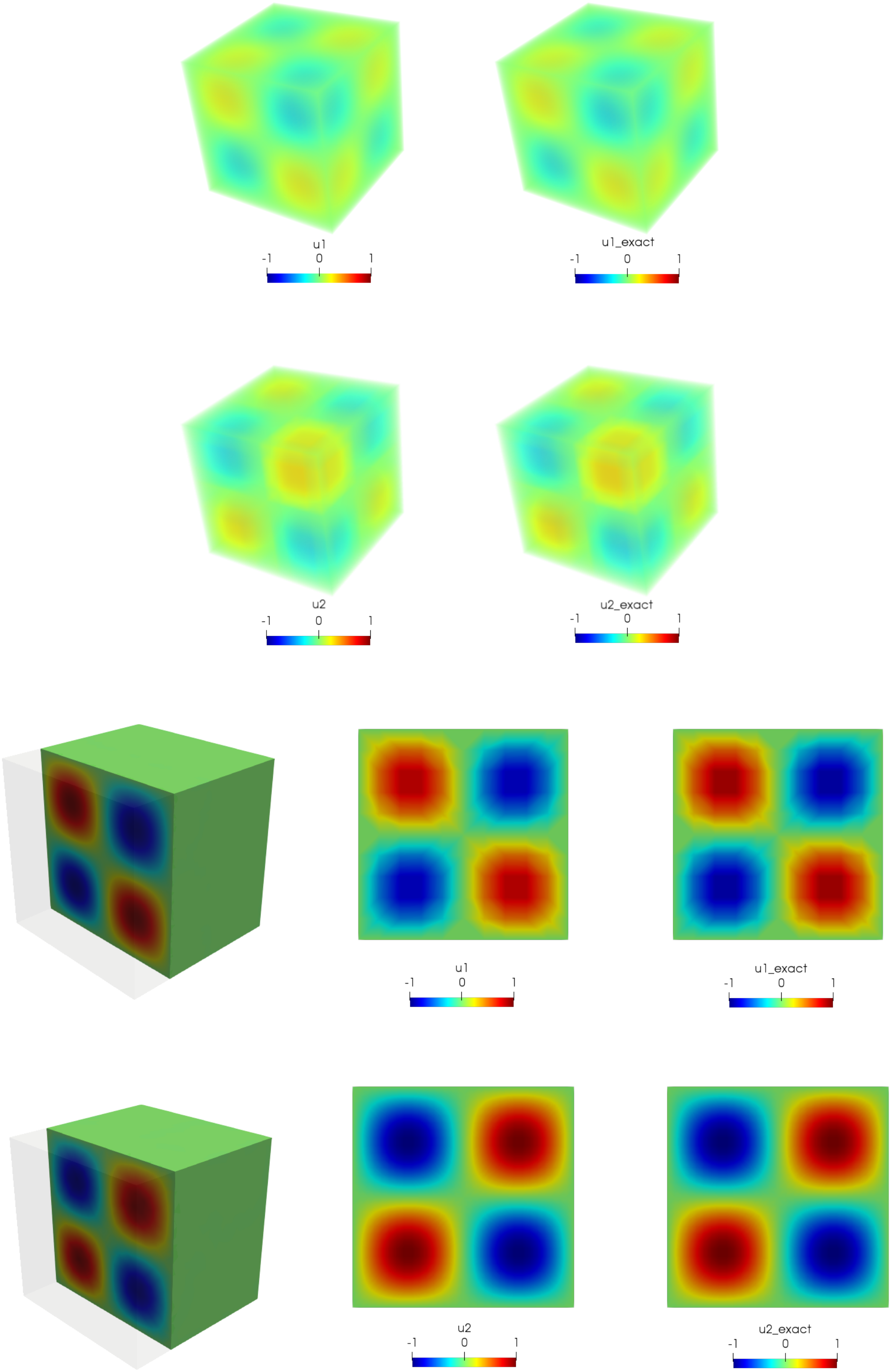

Figure 1: Comparison between numerical and analytical solution for u_1 and u_2 (both volumetric and cut views are shown).

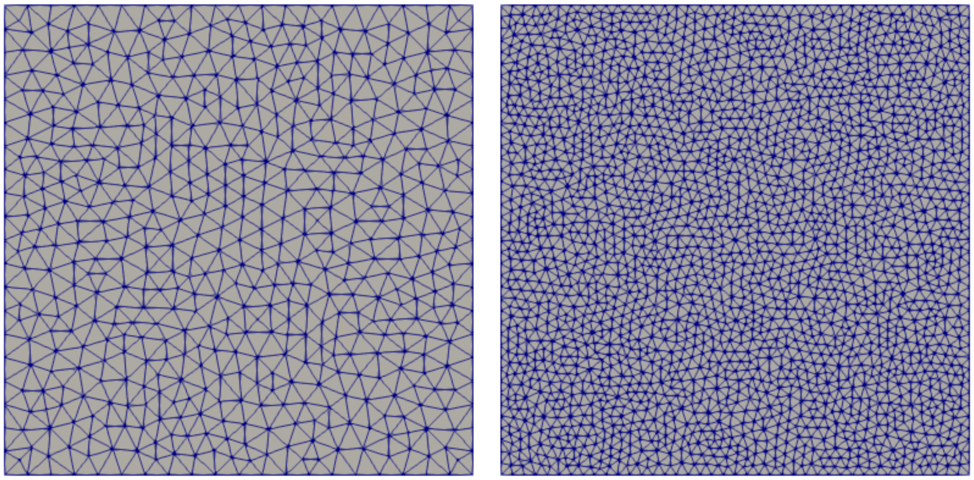

Figure 2: Lateral view of an example of non-nested unstructured meshes comprised of 10’632 elements for u_1 (left) and 247’030 elements for u_2 (right).

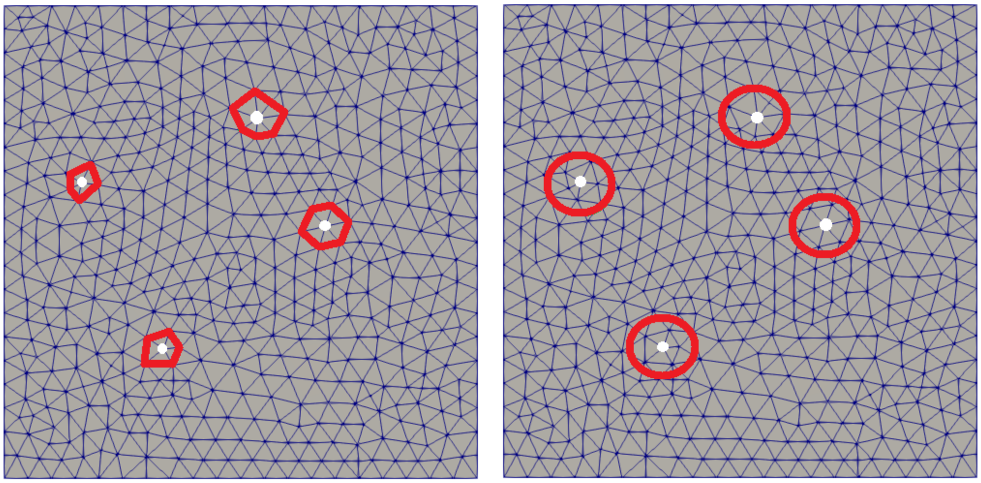

Figure 3: Choice of the support of the RBF by means of the number of links (left) and a fixed radius (right) over an unstructured grid.

$$
\begin{aligned}
f_2 = {} & (1-3\pi^2)\sin(\pi x)\sin(\pi y)\sin(\pi z) + \pi\cos(\pi x)\sin(\pi y)\sin(\pi z) \\
& + \pi\sin(\pi x)\cos(\pi y)\sin(\pi z) + \pi\sin(\pi x)\sin(\pi y)\cos(\pi z).
\end{aligned}
$$

This one-way 2-field coupled system involving Laplace and diffusion-advection-reaction PDEs is well posed and is endowed with an exact solution, $u_1 = \sin(\pi x)\sin(\pi y)\sin(\pi z)$ and $u_2 = -\sin(\pi x)\sin(\pi y)\sin(\pi z)$. We use the Finite Element method to solve numerically this test case. We provide two different meshes $\mathcal{T}_{h_1}$ and $\mathcal{T}_{h_2}$ of the computational domain made by tetrahedrons, with h_1 and h_2 representing the maximum size of the element K in terms of maximum mean diameter of the circumscribed circumference, with $\cup_{K\in\mathcal{T}_{h_1}} K = \cup_{K\in\mathcal{T}_{h_2}} K = \overline{\Omega}$. Both structured and unstructured meshes can be potentially employed, either in a nested or a non-nested fashion. We denote N_{u_1} and N_{u_2} the number of degrees of freedom for u_1 and u_2 respectively (these are the internal finite element nodes). We also introduce two finite dimensional spaces $\mathcal{X}^r_{h_1} = \{v \in C^0(\bar{\Omega}) : v|_K \in \mathcal{P}^r(K) \ \ \forall K \in \mathcal{T}_{h_1}\}$, $\mathcal{X}^r_{h_2} = \{v \in C^0(\bar{\Omega}) : v|_K \in \mathcal{P}^r(K) \ \ \forall K \in \mathcal{T}_{h_2}\}$, for $r \geq 1$. The set of basis functions of $\mathcal{X}^r_{h_1}$ with $N_{u_1} = \dim(\mathcal{X}^r_{h_1})$ is defined by $\{\phi_i\}_{i=1}^{N_{u_1}}$, whereas the ones of $\mathcal{X}^r_{h_2}$ with $N_{u_2} = \dim(\mathcal{X}^r_{h_2})$ are defined by $\{\psi_i\}_{i=1}^{N_{u_2}}$. We call $u_{1,h_1} = \sum_{j=1}^{N_{u_1}} u_{1,j}\phi_j$ and $u_{2,h_2} = \sum_{j=1}^{N_{u_2}} u_{2,j}\psi_j$ the finite element solutions in $V^r_{h_1} = \mathcal{X}^r_{h_1} \cap H^1_0(\Omega)$ and $V^r_{h_2} = \mathcal{X}^r_{h_2} \cap H^1_0(\Omega)$, respectively.

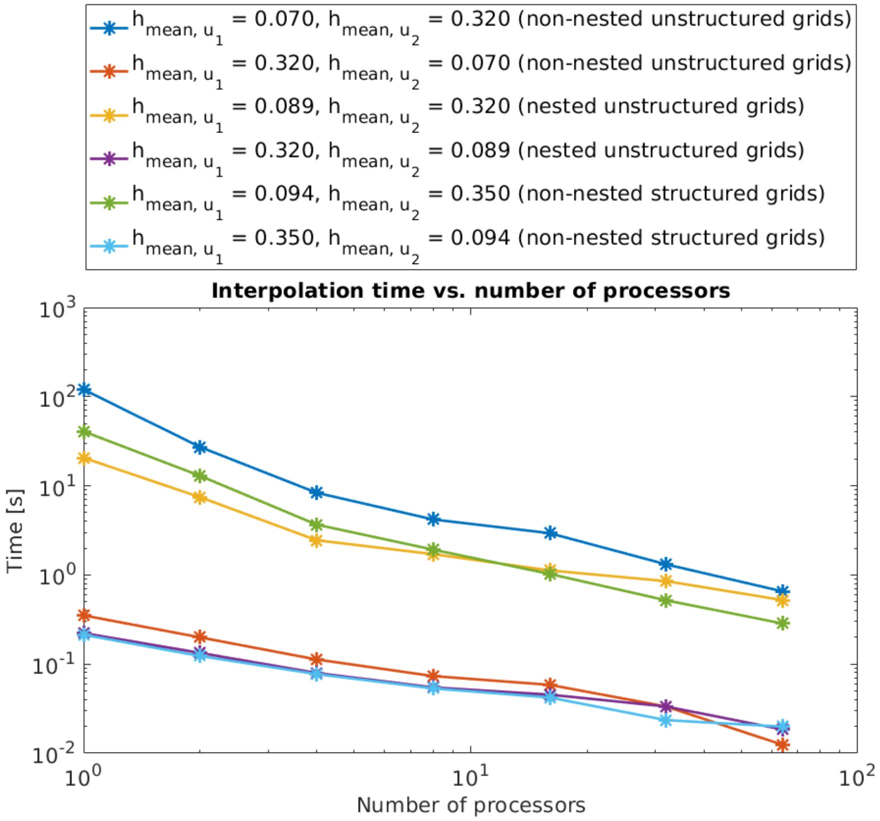

Figure 4: Interpolation CPU time (in seconds) vs. number of processors for different choices of the mesh and the number of elements.

The discretized formulation of (9) reads: find $u_{1,h_1} \in V^r_{h_1}$ and $u_{2,h_2} \in V^r_{h_2}$ such that

$$\begin{cases}\sum_{j=1}^{N_{u_1}} u_{1,j} \int_\Omega \nabla\phi_j \nabla\phi_i = \int_\Omega f_1 \phi_i & \forall i = 1, ..., N_{u_1}, \\ \sum_{j=1}^{N_{u_2}} u_{2,j} \int_\Omega \nabla\psi_j \nabla\psi_i = \int_\Omega \left(f_2 - u_{1,h_2} - \nabla u_{1,h_2} \cdot \boldsymbol{v}\right) \psi_i & \forall i = 1, ..., N_{u_2},\end{cases} \tag{10}$$

where $u_{1,h_2} = \sum_{j=1}^{N_{u_2}} u_{1,j}\psi_j$ is the interpolation of u_{1,h_1} on the second mesh, and again $\boldsymbol{v} = \mathbf{1}$. For this purpose, we use the RL-RBF introduced in Section 2, so that, at a continuous level, $u_{1,h_2}(\boldsymbol{x}) = \bar{\Pi}_{u_1}(\boldsymbol{x})$. In order to take into account the distribution of mesh points of $\mathcal{T}_{h_1}$ and $\mathcal{T}_{h_2}$, we define an adaptive strategy to select the radius of the support of Beckert & Wendland basis functions by means of the number of links that a certain vertex of the mesh has with the surrounding neighborhood. In this way we exploit the structure of the mesh to build a variable and local support of the RBF that keeps into account the level of refinement of the mesh in each region of the computational domain. For more details about this technique we refer to [22]. A number of links equal to 1, as shown in Figure 3, is sufficient to obtain a good interpolated solution. The derivatives of u_{1,h_2} with respect to x, y and z are calculated using the Zienkiewicz-Zhu gradient recovery method [91, 92], which is known to be efficient and superconvergent.

We have performed strong scalability tests and convergence analysis of both L^2 and H^1 errors for u_{1,h_1} and u_{2,h_2}, considering structured, nested unstructured and non-nested unstructured grids. $\mathcal{P}^1$ finite elements are used in all simulations. In Figure 1 we show a comparison over the entire computational domain and over a cross-section of u_{1,h_1} vs. u_1 and u_{2,h_2} vs. u_2, considering, as depicted in Figure 2, two different unstructured grids that are non-nested and providing in both cases a good match of the numerical and analytical solutions. We see that our approach based on a RBF interpolant whose support is chosen by the number of links is able to pass properly the information of u_{1,h_1} inside the equation of u_{2,h_2}. This is confirmed by the fact that the exact solutions u_1 and u_2 match really well the corresponding numerical solutions u_{1,h_1} and u_{2,h_2}. We also test the scalability of our RL-RBF operator, as shown in Figure 4, where we see that the time that we need to interpolate u_{1,h_1} inside the equation for u_{2,h_2} decreases with the number of CPUs with all types of grids. We want to underline that this behaviour is observed in the case the coarse

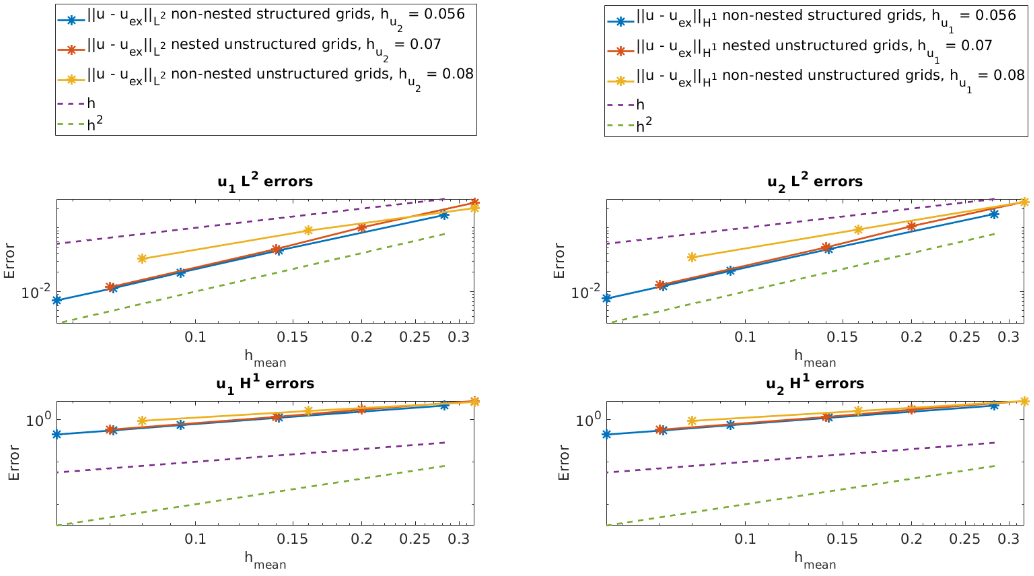

Figure 5: Convergence analysis for L^2 and H^1 errors vs. $h_{u_1,mean}$ with $h_{u_2,mean}$ fixed (left) and viceversa (right).

mesh is used for u_{1,h_1} and the fine one for u_{2,h_2}, and viceversa. Moreover, due to the generality that we want to obtain with our intergrid operator, it seems that, independently of the value of the mesh size, the interpolation process scales better with non-nested unstructured grids.

Grid	$h_{1,mean}$	$h_{2,mean}$	e_{u_1,L^2}	e_{u_1,H^1}	e_{u_2,L^2}	e_{u_2,H^1}
Unstructured	0.32	0.19	0.2469	2.7113	0.1171	1.7207
Unstructured	0.16	0.10	0.0901	1.5778	0.0471	1.0401
Unstructured	0.08	0.05	0.0325	0.9253	0.0255	0.6835
Unstructured	0.19	0.32	0.1008	1.6967	0.2571	2.7302
Unstructured	0.10	0.16	0.0347	0.9739	0.1326	1.8995
Unstructured	0.05	0.08	0.0124	0.5700	0.0763	0.8553
Structured	0.28	0.09	0.1590	2.1149	0.0306	0.7416
Structured	0.14	0.07	0.0440	1.0921	0.0141	0.5527
Structured	0.09	0.06	0.0199	0.7323	0.0086	0.4413
Structured	0.09	0.28	0.0199	0.7323	0.1640	2.1227
Structured	0.07	0.14	0.0113	0.5503	0.0459	1.0939
Structured	0.06	0.09	0.0072	0.4407	0.0210	0.7330

Table 1: Convergence analysis with h_{mean} for u_{1,h_1} and u_{2,h_2} (both unstructured and structured grids are non-nested). $e_{u_1,L^2} = ||u_{1,h_1} - u_1||_{L^2}$, $e_{u_1,H^1} = ||u_{1,h_1} - u_1||_{H^1}$, $e_{u_2,L^2} = ||u_{2,h_2} - u_2||_{L^2}$, $e_{u_2,H^1} = ||u_{2,h_2} - u_2||_{H^1}$.

In Figure 5 we show a convergence analysis of L^2 and H^1 errors where we consider a fixed grid for u_{2,h_2}, with a certain mean diameter of the elements $h_{u_2} = h_{2,mean}$, and we gradually reduce the $h_{u_1} = h_{1,mean}$ value, and viceversa. Table 1 reports the results in case we make a progressive increment of the number of mesh elements for both u_{1,h_1} and u_{2,h_2} in parallel: we start from a certain couple of non-nested unstructured/structured meshes with specific values of $h_{1,mean}$ and $h_{2,mean}$, and then we halve these values and analyse the behaviour of both L^2 and H^1 errors. We highlight that the order of convergence that we expect theoretically (i.e 1 for the H^1 norm error and 2 for the L^2 norm error) is always recovered for every mesh used.

4 Cardiac electromechanics

Now we apply the approach developed and tested in Sections 2 and 3 to solve the cardiac electromechanics problem.

4.1 Mathematical model

Heart tissue is made of cardiomyocytes, which determines the orthotropic structure of the left ventricle through the organization in fibers and laminar collagen sheets [76]. In this section, we review the model governing the electromechanical behaviour of the left ventricle by accounting the characteristics of myocardium [26].

4.1.1 Electrophysiology

The contraction of a single cardiac cell is initiated by an electric activation due to an action potential, a depolarizing phase that raises the so called transmembrane potential of an excitable cell from its resting value ranging between -90 and -80 mV to slightly positive values, followed by a peak, a plateau, and a repolarization, that returns the transmembrane potential to its resting value [19, 20]. The electric activity of the heart starts at the so called sinoatrial (SA) node and propagates throughout the right atrium [20]. Thanks to the Bachmann's bundle and some other preferential lines of trasmission, the electric signal reaches the left atrium [19]. Then, the activation front arrives at the atrioventricular (AV) node, which conducts the action potential through the nonexcitable atrioventricular septum, activating the specialized fibers of the bundle of His and the Purkinje network, that spreads as a tree-like left and right bundle branches ending on the endocardial surface of the ventricles. These Purkinje terminations transmit the action potentials to the ventricular walls and cardiac excitation then propagates throughout the ventricles [47, 75].

The monodomain model is a diffusion-reaction PDE system able to describe the electric properties of cardiac muscle cells, assuming the same anisotropy ratios between the intracellular and extracellular spaces [58, 73]. It is a continuum model, which means that it is used to capture average properties of many cardiomyocytes, and not the behaviour of single cells. In physiological conditions, the monodomain model reads:

$$\begin{cases} \chi\big[C_m \dfrac{\partial u}{\partial t} + I_{ion}(u, \boldsymbol{z})\big] = \nabla \cdot (J\boldsymbol{F}^{-1}\boldsymbol{D_M}\boldsymbol{F}^{-T}\nabla u) + I_{app}(t) & \text{in } \Omega_0 \times (0,T), \\ \big(J\boldsymbol{F}^{-1}\boldsymbol{D_M}\boldsymbol{F}^{-T}\nabla u\big) \cdot \boldsymbol{N} = 0 & \text{on } \partial\Omega_0 \times (0,T), \\ u = u_0 & \text{in } \Omega_0 \times \{0\}. \end{cases} \tag{11}$$

$\Omega_0 \subset \mathbb{R}^3$ is the domain in the reference configuration, represented in our case by an idealized left ventricle at the end of the diastolic phase. $T > 0$ is the final time. C_m is the total membrane capacitance and χ is the area of cell membrane per tissue volume. u is the dimensionless transmembrane potential, whereas the vector $\boldsymbol{z} = \{z_1, z_2, ..., z_k\}$ expresses k recovery (or gating) variables, which play the role of probability density functions and model the fraction of open ionic channels across the membrane of a single cell. $\boldsymbol{D_M} = \sigma_t \boldsymbol{I} + (\sigma_l - \sigma_t)\boldsymbol{f_0} \otimes \boldsymbol{f_0}$ refers to the diffusion tensor, being $\boldsymbol{f_0}$ the vector field expressing the fibers direction and $\sigma_l, \sigma_t \in \mathbb{R}^+$ the longitudinal and transversal conductivities respectively [71]. By defining $\boldsymbol{X}$ and $\boldsymbol{x}$ as the reference and deformed coordinates, we introduce the deformation tensor $\boldsymbol{F} = \boldsymbol{I} + \dfrac{\partial \boldsymbol{d_s}}{\partial \boldsymbol{X}}$ (with $J = \det(\boldsymbol{F}) > 0$), keeping into account the effect of the mechanical displacement $\boldsymbol{d_s}$ on the electrophysiology. $I_{app}(t)$ is an external applied current, which should simulate in our case the behaviour of the Purkinje network. Indeed we use it to trigger the action potential in specific points of the myocardium. $I_{ion}(u, \boldsymbol{z})$ is the feedback from the cellular scale into the tissue one, and strictly depends on the chosen ionic model. A Neumann boundary condition is applied all over the boundary and defines the condition of electrically isolated domain.

In literature there are several possible choices of ionic models [1, 46, 84]. We present here the monodomain equation supplemented by the Bueno-Orovio minimal ionic model, which is specifically designed for the human left ventricle to describe from a phenomenological perspective the microscopical details of each single cardiomyocyte [10]:

$$\begin{cases} \dfrac{\partial u}{\partial t} + I_{ion}(u, \boldsymbol{z}) = \nabla \cdot (J\boldsymbol{F}^{-1}\boldsymbol{D_M}\boldsymbol{F}^{-T}\nabla u) + I_{app}(t) & \text{in } \Omega_0 \times (0,T), \\ \dfrac{\partial v}{\partial t} = \dfrac{(1 - H(u-\theta_v))(v_\infty - v)}{\tau_v^-} - \dfrac{H(u-\theta_v)v}{\tau_v^+} & \text{in } \Omega_0 \times (0,T), \\ \dfrac{\partial w}{\partial t} = \dfrac{(1 - H(u-\theta_w))(w_\infty - w)}{\tau_w^-} - \dfrac{H(u-\theta_w)w}{\tau_w^+} & \text{in } \Omega_0 \times (0,T), \\ \dfrac{\partial s}{\partial t} = \dfrac{1}{\tau_s}\left(\dfrac{1 + \tanh(k_s(u - u_s))}{2} - s\right) & \text{in } \Omega_0 \times (0,T), \\ \big(J\boldsymbol{F}^{-1}\boldsymbol{D_M}\boldsymbol{F}^{-T}\nabla u\big) \cdot \boldsymbol{N} = 0 & \text{on } \partial\Omega_0 \times (0,T), \\ u = u_0,\ v = v_0,\ w = w_0,\ s = s_0 & \text{in } \Omega_0 \times \{0\}, \end{cases} \tag{12}$$

where $C_m = \chi = 1$, $H(x - x_0)$ is an Heaviside function centered at x_0, $\boldsymbol{z} = \{v, w, s\}$ is the vector of gating variables and evolves over the time thanks to a system of 3 ODEs, which are solved at each point of the reference domain. The

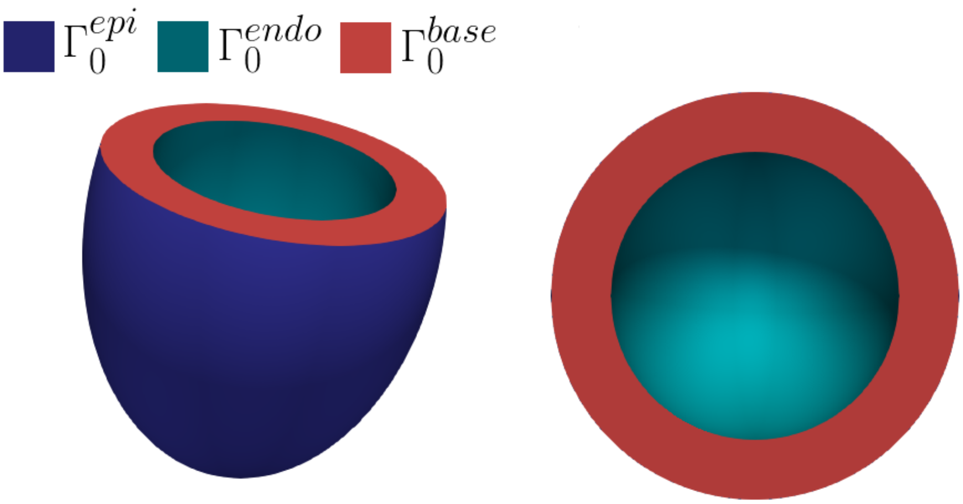

Figure 6: Geometry of the prolate ellipsoidal. Lateral view (left) and view from above (right).

ionic current $I_{ion}(u, \boldsymbol{z})$ is given by:

$$
\begin{aligned}
I_{ion}(u, \boldsymbol{z}) = &- \frac{vH(u-\theta_v)(u-\theta_v)(u_u-u)}{\tau_{fi}} \\
&+ \frac{(u-u_0)(1-H(u-\theta_w))}{\tau_0} + \frac{H(u-\theta_w)}{\tau_{so}} - \frac{H(u-\theta_w)ws}{\tau_{si}}.
\end{aligned}
$$

4.1.2 Mechanical activation

The mechanical activation bridges electrophysiology and passive mechanics. We consider a phenomenological model that keeps into account the local shortening of the fibers γ_f at the macroscopical level [33, 67, 70]. In this way we are able to describe the behaviour of the fibers in a faster but more approximated way, with respect to more complex and accurate models that are able to describe the dynamic of sarcomeres [64]. Myocardial displacement feedback $\boldsymbol{d_s}$ and concentration of calcium ions Ca^{2+} play an important role in the time evolution of γ_f. As already done in literature [33, 67, 68], the gating variable s substitutes the concentration of Ca^{2+}, due to the fact that they have a pointwise similar time pattern, even if the order of magnitude is different. The formulation is the following:

$$
\begin{cases}
\dfrac{\partial \gamma_f}{\partial t} - \dfrac{\varepsilon}{g(s)} \Delta \gamma_f = \dfrac{1}{g(s)} \Phi(s, \gamma_f, \boldsymbol{d_s}) & \text{in } \Omega_0 \times (0, T), \\
\nabla \gamma_f \cdot \boldsymbol{N} = 0 & \text{on } \partial\Omega_0 \times (0, T), \\
\gamma_f = 0 & \text{in } \Omega_0 \times \{0\},
\end{cases}
\tag{13}
$$

where $g(s) = \mu_A s^2$, $\Phi(s, \gamma_f, \boldsymbol{d_s}) = \alpha H_{s_0}(s)(s-s_0)^2 R_{FL}(I_{4f}) + \sum_{j=1}^{5}(-1)^j(j+1)(j+2)I_{4f}\gamma_f^j$ is the active force, $R_{FL}(x) = \chi_{[SL_{min}, SL_{max}]}(\sqrt{x}l_0)\Big\{\frac{d_0}{2} + \sum_{n=1}^{3}[d_n \mathrm{sin}(\sqrt{x}l_0) + e_n \mathrm{cos}(\sqrt{x}l_0)]\Big\}$ is a truncated Fourier series expressing the sarcomere force-length relationship [37]. Both α and μ_A should be calibrated according to the specific case under investigation. The active deformation is calculated exploiting the following orthotropic form [2]:

$$
\boldsymbol{F_A} = \boldsymbol{I} + \gamma_f \boldsymbol{f_0} \otimes \boldsymbol{f_0} + \gamma_s \boldsymbol{s_0} \otimes \boldsymbol{s_0} + \gamma_n \boldsymbol{n_0} \otimes \boldsymbol{n_0},
\tag{14}
$$

where $\boldsymbol{s_0}$ and $\boldsymbol{n_0}$ represent the sheets and their normal direction respectively, with γ_s and γ_n corresponding local shortening or elongation [7, 52]:

$$
\gamma_n = \bar{k}' \left(\bar{k}_{endo} \frac{\lambda - \lambda_{epi}}{\lambda_{endo} - \lambda_{epi}} + \bar{k}_{epi} \frac{\lambda - \lambda_{endo}}{\lambda_{epi} - \lambda_{endo}} \right) \left(\frac{1}{\sqrt{1+\gamma_f}} - 1 \right),
\tag{15}
$$

$$
\gamma_s = \frac{1}{(1+\gamma_f)(1+\gamma_n)} - 1.
\tag{16}
$$

Here λ represents a transmural coordinate, varying from λ_{endo} at the endocardium to λ_{epi} at the epicardium, which permits to have a transversely non-homogeneous thickening of the left ventricular wall. γ_s is set like (16) yield to $\det(\boldsymbol{F_A}) = 1$.

4.1.3 Active and passive mechanics

In order to describe the displacement of the myocardium along the entire heartbeat, we model the properties of the tissue by means of fibers $\boldsymbol{f_0}$, sheets $\boldsymbol{s_0}$ and their normals $\boldsymbol{n_0}$, which permit to obtain highly anisotropic internal stresses associated with a prescribed deformation [39]. We use a nearly-incompressible formulation by weakly penalizing large volumetric variations [77]. Moreover, the dimensionless variable γ_f provides a link between electrophysiology and mechanics. The momentum conservation equation with boundary and initial conditions reads [51]:

$$\begin{cases} \rho_s \dfrac{\partial^2 \boldsymbol{d_s}}{\partial t^2} - \nabla \cdot \boldsymbol{P}(\boldsymbol{d_s}, \gamma_f) = \boldsymbol{0} & \text{in } \Omega_0 \times (0, T), \\ (\boldsymbol{N} \otimes \boldsymbol{N}) \left(K_\perp^{epi} \boldsymbol{d_s} + C_\perp^{epi} \dfrac{\partial \boldsymbol{d_s}}{\partial t} \right) & \\ \quad + (\boldsymbol{I} - \boldsymbol{N} \otimes \boldsymbol{N}) \left(K_\parallel^{epi} \boldsymbol{d_s} + C_\parallel^{epi} \dfrac{\partial \boldsymbol{d_s}}{\partial t} \right) + \boldsymbol{P}(\boldsymbol{d_s}, \gamma_f)\boldsymbol{N} = 0 & \text{on } \Gamma_0^{epi} \times (0, T), \\ \boldsymbol{P}(\boldsymbol{d_s}, \gamma_f)\boldsymbol{N} = 0 & \text{on } \Gamma_0^{base} \times (0, T), \\ \boldsymbol{P}(\boldsymbol{d_s}, \gamma_f)\boldsymbol{N} = -p^{endo}(t)\boldsymbol{N} & \text{on } \Gamma_0^{endo} \times (0, T), \\ \boldsymbol{d_s} = \boldsymbol{d_{s,0}}, \ \dfrac{\partial \boldsymbol{d_s}}{\partial t} = \dot{\boldsymbol{d}}_{\boldsymbol{s,0}} & \text{in } \Omega_0 \times \{0\}. \end{cases} \tag{17}$$

A Robin boundary condition is prescribed at the epicardium to account for the action of the pericardial sac, so that the presence of the pericardium is also addressed and modelled [57]. $K_\perp^{epi}$, $K_\parallel^{epi}$, $C_\perp^{epi}$, $C_\parallel^{epi} \in \mathbb{R}^+$ are respectively local values of stiffness and viscosity constants of the epicardial tissue in the normal or tangential directions. A Neumann boundary condition is defined at the base and acts as a free contraction condition. $p^{endo}(t)$ is the internal pressure of the ventricular chamber and is modelled through a 0D model, as will be detailed in subsection 4.1.5. The Piola-Kirchhoff strain tensor $\boldsymbol{P} = \boldsymbol{P}(\boldsymbol{d_s}, \gamma_f)$ incorporates both the passive and active mechanical properties of the tissue. After defining the symmetric positive definite right Cauchy-Green tensor $\boldsymbol{C} = \boldsymbol{F}^T \boldsymbol{F}$, with $\boldsymbol{F} = \boldsymbol{I} + \nabla \boldsymbol{d_s}$ deformation tensor, the strain energy function $\mathcal{W} : \mathbb{R}^{3x3} \to \mathbb{R}$ provides a link between the strain and the energy of the material. Under the hyperelasticity assumption, the strain energy function can be differentiated with respect to the deformation tensor $\boldsymbol{F}$ in order to obtain $\boldsymbol{P}$:

$$\boldsymbol{P}(\boldsymbol{d_s}, \gamma_f) = \frac{\partial \mathcal{W}(\boldsymbol{C})}{\partial \boldsymbol{F}}. \tag{18}$$

There are several models in literature which are able to describe the anisotropic nature of the tissue, such as the Guccione [38] or the Holzapfel-Ogden laws [40]. We use the second one, which formulates the following additive decomposition of the strain energy function:

$$\begin{aligned} \mathcal{W}(\boldsymbol{C}) &= \mathcal{W}_1(\mathcal{I}_1) + \mathcal{W}_{4f}(\mathcal{I}_{4f}) + \mathcal{W}_{4s}(\mathcal{I}_{4s}) + \mathcal{W}_{8fs}(\mathcal{I}_{8fs}) \\ &= \frac{a}{2b} e^{b(\mathcal{I}_1 - 3)} + \frac{a_f}{2b_f} \left[e^{b_f < \mathcal{I}_{4f} - 1 >^2} - 1 \right] + \frac{a_s}{2b_s} \left[e^{b_s < \mathcal{I}_{4s} - 1 >^2} - 1 \right] \\ &+ \frac{a_{fs}}{2b_{fs}} \left[e^{b_{fs} \mathcal{I}_{8fs}^2} - 1 \right], \end{aligned} \tag{19}$$

where $\mathcal{I}_1 = tr(\boldsymbol{C})$, $\mathcal{I}_{4f} = \boldsymbol{C} : \boldsymbol{f_0} \otimes \boldsymbol{f_0}$, $\mathcal{I}_{4s} = \boldsymbol{C} : \boldsymbol{s_0} \otimes \boldsymbol{s_0}$, $\mathcal{I}_{8fs} = \boldsymbol{C} : \boldsymbol{f_0} \otimes \boldsymbol{s_0}$ are the invariants of the right Cauchy-Green tensor. a_k, b_k coefficients are fitted from experimental data [40]. The function $< y >= y H_0(y)$, with $H_0(y)$ Heaviside function centered in 0, indicates the positive part of y and permits to switch off the effects of both fibers and sheets when they are under compression. We introduce a convex term $\mathcal{W}_{vol}(J) = \dfrac{B}{2}(J-1)log(J)$ into the strain energy function $\mathcal{W}$ such that $J = 1$ is its global minimum. In this way, we are able to set the nearly-incompressible constraint [18, 23, 90]. $B \in \mathbb{R}^+$ is the bulk modulus, which has a role both in the torsion mechanism of the ventricle and incompressibility constraint [33]. Following [74], we model the evaluation of the isotropic term $\mathcal{W}_1$ in $J^{-\frac{2}{3}}\mathcal{I}_1$ and not directly in the first invariant.

We now move towards the active part, which is due to the electrical impulse and is formulated in the active strain framework [2, 3, 49, 67]. In addition to the reference configuration Ω_0 and the deformed one Ω, we introduce an intermediate state $\hat{\Omega}$, which represents the active part of the deformation. By means of the 2^{nd} order tensor $\boldsymbol{F}_A$, we map Ω_0 into $\hat{\Omega}$, whereas the $\boldsymbol{F}_E$ tensor takes the role to finally transform $\hat{\Omega}$ into Ω. We finally reach, the multiplicative decomposition of $\boldsymbol{F} = \boldsymbol{F}_E \boldsymbol{F}_A$. The first Piola-Kirchhoff strain tensor $\boldsymbol{P}$ reads:

$$\boldsymbol{P} = \det(\boldsymbol{F}_A) \boldsymbol{P}_E {\boldsymbol{F}_A}^{-T}, \qquad \boldsymbol{P}_E = \frac{\partial \mathcal{W}(\boldsymbol{C}_E, J)}{\partial \boldsymbol{F}_E}. \tag{20}$$

For additional details on the final form of tensor $\boldsymbol{P}$, we refer the reader to [33].

4.1.4 The multifield coupled problem

The fully coupled multifield electromechanical problem is presented here below:

$$\begin{cases}
\chi\big[C_m \dfrac{\partial u}{\partial t} + I_{ion}(u,v,w,s)\big] = \nabla\cdot(J\boldsymbol{F}^{-1}\boldsymbol{D_M}\boldsymbol{F}^{-T}\nabla u) + I_{app}(t) & \text{in } \Omega_0\times(0,T),\\
\dfrac{\partial v}{\partial t} = \dfrac{(1-H(u-\theta_v))(v_\infty - v)}{\tau_v^-} - \dfrac{H(u-\theta_v)v}{\tau_v^+} & \text{in } \Omega_0\times(0,T),\\
\dfrac{\partial w}{\partial t} = \dfrac{(1-H(u-\theta_w))(w_\infty - w)}{\tau_w^-} - \dfrac{H(u-\theta_w)w}{\tau_w^+} & \text{in } \Omega_0\times(0,T),\\
\dfrac{\partial s}{\partial t} = \dfrac{1}{\tau_s}\left(\dfrac{1+\tanh(k_s(u-u_s))}{2} - s\right) & \text{in } \Omega_0\times(0,T),\\
\dfrac{\partial \gamma_f}{\partial t} - \dfrac{\varepsilon}{g(s)}\Delta\gamma_f = \dfrac{1}{g(s)}\Phi(s,\gamma_f,\boldsymbol{d_s}) & \text{in } \Omega_0\times(0,T),\\
\rho_s\dfrac{\partial^2 \boldsymbol{d_s}}{\partial t^2} - \nabla\cdot\boldsymbol{P}(\boldsymbol{d_s},\gamma_f) = \boldsymbol{0} & \text{in } \Omega_0\times(0,T),\\
\big(J\boldsymbol{F}^{-1}\boldsymbol{D_M}\boldsymbol{F}^{-T}\nabla u\big)\cdot\boldsymbol{N} = 0 & \text{on } \partial\Omega_0\times(0,T),\\
\nabla\gamma_f\cdot\boldsymbol{N} = 0 & \text{on } \partial\Omega_0\times(0,T),\\
(\boldsymbol{N}\otimes\boldsymbol{N})\left(K_\perp^{epi}\boldsymbol{d_s} + C_\perp^{epi}\dfrac{\partial \boldsymbol{d_s}}{\partial t}\right) & \\
\quad + (\boldsymbol{I}-\boldsymbol{N}\otimes\boldsymbol{N})\left(K_\parallel^{epi}\boldsymbol{d_s} + C_\parallel^{epi}\dfrac{\partial \boldsymbol{d_s}}{\partial t}\right) + \boldsymbol{P}(\boldsymbol{d_s},\gamma_f)\boldsymbol{N} = 0 & \text{on } \Gamma_0^{epi}\times(0,T),\\
\boldsymbol{P}(\boldsymbol{d_s},\gamma_f)\boldsymbol{N} = 0 & \text{on } \Gamma_0^{base}\times(0,T),\\
\boldsymbol{P}(\boldsymbol{d_s},\gamma_f)\boldsymbol{N} = -p^{endo}(t)\boldsymbol{N} & \text{on } \Gamma_0^{endo}\times(0,T),\\
u = u_0,\ v = v_0,\ w = w_0,\ s = s_0 & \text{in } \Omega_0\times\{0\},\\
\gamma_f = \gamma_{f,0} & \text{in } \Omega_0\times\{0\},\\
\boldsymbol{d_s} = \boldsymbol{d_{s,0}},\ \dfrac{\partial \boldsymbol{d_s}}{\partial t} = \dot{\boldsymbol{d}}_{\boldsymbol{s,0}} & \text{in } \Omega_0\times\{0\},
\end{cases} \tag{21}$$

where $p^{endo}(t)$ is the unknown of a 0D fluid problem that changes over the time with the different phases that involve a physiological heartbeat.

4.1.5 Cardiac cycle

We model the evolution of both endocardial pressure and volume along the heartbeat, considering a total duration $T = 0.8$ s. With this aim, we consider ordinary differential equations to model the fluid in the left ventricle chamber, where we assume that the endocardial pressure is uniform over the domain. The heartbeat is conventionally split into four phases, in which we solve four different ODEs [33]:

- Isovolumetric contraction: increase of p^{endo} from the End Diastolic Pressure (EDP, about 10 mmHg) to the aortic pressure (about 85 mmHg) while the volume V^{endo} remains almost constant, according to the following equation:

  $$\frac{dV^{endo}}{dt}(p^{endo}) = 0 \quad t\in(0,T_1], \tag{22}$$

  where V^{endo} is set to the initial volume, and $T_1 = T_1(p^{endo})$ is the earliest occurrence in time at which $p^{endo} \geq p^{ao}$, that forces the aortic valve opening.

- Ejection: the left ventricle contracts and pushes blood to flow through the aortic valve, which closes itself at the end of this phase (when $p^{endo} \leq p^{ao}$). V^{endo} decreases following a two 0D element Windkessel model [89]:

  $$C\frac{dp^{endo}}{dt} = -\frac{p^{endo}}{R} - \frac{dV^{endo}}{dt} \quad t\in(T_1,T_2], \tag{23}$$

  with $p^{endo}(T_1) = p^{ao}$, $C, R > 0$ are two parameters representing the capacitance and the resistance of the electric circuit that mimics the blood flowing in the aorta. $T_2 = T_2(V^{endo})$ is the first instant of time in which $\dfrac{dV^{endo}}{dt} \geq 0$.

- Isovolumetric relaxation: decrease of p^{endo} with constant value of V^{endo}, treated from the mathematical perspective in the same way as the isovolumetric contraction. $T_3 = T_3(p^{endo})$ is the first occurrence in time at which $p^{endo} \leq p^{endo}_{min} = 5$ mmHg.
- Filling: the mitral valve opens due to the pressure drop, blood flows inside the left ventricle causing an increment of V^{endo} until both p^{endo} and V^{endo} attain the EDP values. We increase linearly p^{endo} until it reaches the initial value p^{endo}_{EDP} at $\bar{T}_3 = 0.7\ s$ and we keep it constant from $\bar{T}_3$ to the final time $T = 0.8\ s$ by setting:

  $$\frac{dp^{endo}}{dt} = \xi \quad t \in (T_3, T), \tag{24}$$

  where

  $$\begin{cases} \xi = \dfrac{p^{endo}_{EDP} - p^{endo}(T_3)}{\bar{T}_3 - T_3} & \text{if } t \in (T_3, \bar{T}_3], \\ \xi = 0 & \text{otherwise.} \end{cases} \tag{25}$$

The endocardial volume $V^{endo}(t)$ is computed exploiting the following formula:

$$V^{endo}(t) = \int_{\Gamma_0^{endo}} J(\boldsymbol{d_s}(t))\boldsymbol{\xi} \cdot \boldsymbol{F}^{-T}(\boldsymbol{d_s}(t))\boldsymbol{N} d\Gamma_0, \tag{26}$$

which is derived in [66], with $\boldsymbol{\xi}$ vector directed in the normal direction of the LV base.

4.2 Numerical discretization

In this section we numerically discretize system (21) using the Finite Element Method in space and Backward Differentiation Formula in time. Our numerical method permits to separate and manage properly the space and time scales related to cardiac electromechanics. We try to reduce at maximum the number of interpolations of the fields defined on different grids and the number of time advancements of the different physics while preserving accuracy and stability.

4.2.1 Space discretization

We provide two meshes $\mathcal{T}_{h_1}$ and $\mathcal{T}_{h_2}$ of the computational domain made of tetrahedrons. h_1 and h_2 (with $h_1 < h_2$) represent the maximum size of the element K, say the maximum of the mean diameter of the circumscribed circumference. $\mathcal{T}_{h_1}$, which is the fine mesh, is used for electrophysiology. The coarser $\mathcal{T}_{h_2}$ mesh is employed for both activation and mechanics. This is motivated by the fact that we need a higher resolution for the electric part, going down to the cellular level, whereas both cardiac mechanics and activation evolve on larger space scales. The geometry for the LV is represented by a prolate ellipsoid (as often done in literature [26, 33, 38, 66]). We denote by N_u, $N_{\boldsymbol{z}}$, N_{γ_f} and $N_{\boldsymbol{d_s}}$ the number of degrees of freedom (DOFs) for dimensionless transmembrane potential, gating variables, mechanical activation and displacement respectively. We define the set of polynomials with degree smaller than or equal to r over an element K of the mesh with $\mathcal{P}^r(K)$, and we introduce the finite dimensional spaces $\mathcal{X}^r_{h_1} = \{v \in C^0(\bar{\Omega}_0) : v|_K \in \mathcal{P}^r(K) \ \ \forall K \in \mathcal{T}_{h_1}\}$ and $\mathcal{X}^r_{h_2} = \{v \in C^0(\bar{\Omega}_0) : v|_K \in \mathcal{P}^r(K) \ \ \forall K \in \mathcal{T}_{h_2}\}$, for $r \geq 1$.

Monodomain model The set of basis functions of $\mathcal{X}^r_{h_1}$ with N_u =dim($\mathcal{X}^r_{h_1}$) is defined by $\{\phi_i\}_{i=1}^{N_u}$. The semidiscretized formulation of the Monodomain equation reads: find $u_{h_1}(t) \in \mathcal{X}^r_{h_1}$ $\forall t \in (0,T)$ such that

$$\begin{aligned} &\int_{\Omega_0} \dot{u}_{h_1}\phi_i d\Omega_0 + \int_{\Omega_0} (J\boldsymbol{F}^{-1}_{h_1}(\boldsymbol{d}_{\boldsymbol{s},h_1})\boldsymbol{D}_m\boldsymbol{F}^{-T}_{h_1}(\boldsymbol{d}_{\boldsymbol{s},h_1})\nabla u_{h_1}) \cdot \nabla\phi_i d\Omega_0 \\ &+ \int_{\Omega_0} I_{ion}(u_{h_1}, \boldsymbol{z}_{h_1})\phi_i d\Omega_0 = \int_{\Omega_0} I_{app}(t)\phi_i d\Omega_0 \quad \forall i = 1, ..., N_u, \end{aligned} \tag{27}$$

with $u_{h_1}(0) = \sum_{j=1}^{N_u}(u_0, \phi_j)_{L^2(\Omega_0)}\phi_j$. $\boldsymbol{z}_{h_1} = \boldsymbol{z}_{h_1}(t)$ and $\boldsymbol{F}_{h_1}$ are the semidiscretized versions of the gating variables and the interpolated deformation tensor respectively, whereas $u_{h_1} = u_{h_1}(t) = \sum_{j=1}^{N_u} u_j(t)\phi_j$ is the finite element solution that approximates u=$u(t)$.

$\boldsymbol{F}_{h_1}$ is obtained with the following procedure:

- RL-RBF are employed for the interpolation of $\boldsymbol{d}_{\boldsymbol{s},h_2}$, which is obtained from (17). The interpolant $\bar{\Pi}_{\boldsymbol{d_s}}(\boldsymbol{x})$ is built on $\mathcal{T}_{h_2}$ and it is used to obtain $\boldsymbol{d}_{\boldsymbol{s},h_1}$ on $\mathcal{T}_{h_1}$ following the procedure explained in Section 2 and exploiting formula (5).

- We get $\boldsymbol{F}_{h_1} = \boldsymbol{I} + \nabla \boldsymbol{d}_{\boldsymbol{s},h_1}$ through the adaptation of the Zienkiewicz-Zhu gradient recovery method [91, 92] to the tensor case.

We can rewrite equation (27) as a system of non linear ODEs by setting $\boldsymbol{u}_{h_1}(t) = \{u_{j,h_1}(t)\}_{j=1}^{N_u}$:

$$\begin{cases} \mathcal{M}\dot{\boldsymbol{u}}_{h_1}(t) + \mathcal{K}(\boldsymbol{d}_{\boldsymbol{s}}(t))\boldsymbol{u}_{h_1}(t) + \boldsymbol{I}_{ion}(\boldsymbol{u}_{h_1}(t), \boldsymbol{z}_{h_1}(t)) = \boldsymbol{I}_{app}(t) \quad \forall t \in (0,T), \\ \boldsymbol{u}_{h_1}(0) = \boldsymbol{u}_{0,h_1}, \end{cases} \tag{28}$$

where $\mathcal{M}_{ij} = \int_{\Omega_0} \phi_j \phi_i d\Omega_0$, $\mathcal{K}_{ij}(\boldsymbol{d}_{\boldsymbol{s}}(t)) = \int_{\Omega_0} (J\boldsymbol{F}_{h_1}^{-1}\boldsymbol{D}_m\boldsymbol{F}_{h_1}^{-T}\nabla\phi_j) \cdot \nabla\phi_i d\Omega_0$ and:

$$\left(\boldsymbol{I}_{ion}(\boldsymbol{u}_{h_1}(t), \boldsymbol{z}_{h_1}(t))\right)_i = \int_{\Omega_0} I_{ion}(u_{h_1}, \boldsymbol{z}_{h_1})\phi_i d\Omega_0,$$
$$\left(\boldsymbol{I}_{app}(t)\right)_i = \int_{\Omega_0} I_{app}(t)\phi_i d\Omega_0.$$

In order to avoid numerical instabilities, we use a lumped $\mathcal{M}_L$ approximation of the mass matrix $\mathcal{M}$ [12]. There are several strategies in literature for the treatment of the non linear term $\boldsymbol{I}_{ion}(\boldsymbol{u}_{h_1}(t), \boldsymbol{z}_{h_1}(t))$ [33, 43, 53, 54, 55]. We use the so-called state variable interpolation (SVI) approach. By denoting with $\{\boldsymbol{x}_s^K\}_{s=1}^{N_q}$ and $\{\omega_s^K\}_{s=1}^{N_q}$ the quadrature nodes and weights of a generic element of the mesh $K \in \mathcal{T}_{h_1}$, both u_{h_1} and $\boldsymbol{z}_{h_1}$ are evaluated at the quadrature nodes as follows:

$$\begin{aligned} &\int_{\Omega_0} I_{ion}(u_{h_1}, \boldsymbol{z}_{h_1})\phi_i d\Omega_0 \\ &\qquad \approx \sum_{K \in \mathcal{T}_{h_1}} \left(\sum_{s=1}^{N_q} I_{ion} \left(\sum_{j=1}^{N_u} u_j(t)\phi_j(\boldsymbol{x}_s^K), \sum_{j=1}^{N_u} \boldsymbol{z}_j(t)\phi_j(\boldsymbol{x}_s^K) \right) \phi_i(\boldsymbol{x}_s^K)\omega_s^K \right). \end{aligned} \tag{29}$$

Bueno-Orovio ionic model The ionic model is a system of ODEs which indirectly depends on the space variable through the transmembrane potential u. The set of degrees of freedom (DOFs) is denoted by $\{\boldsymbol{x}_j\}_{j=1}^{N_{\boldsymbol{z}}}$. The vector of gating variables is rearranged as follows:

$$\boldsymbol{z}_{h_1}(t) = \{\boldsymbol{v}_{h_1}(t), \boldsymbol{w}_{h_1}(t), \boldsymbol{s}_{h_1}(t)\}, \tag{30}$$

with $\boldsymbol{v}_{h_1}(t) = \{v_{j,h_1}(t)\}_{j=1}^{N_{\boldsymbol{z}}}$, $\boldsymbol{w}_{h_1}(t) = \{w_{j,h_1}(t)\}_{j=1}^{N_{\boldsymbol{z}}}$, $\boldsymbol{s}_{h_1}(t) = \{s_{j,h_1}(t)\}_{j=1}^{N_{\boldsymbol{z}}}$. The semi-discrete formulation can be written as follows:

$$\begin{cases} \dot{\boldsymbol{z}}_{h_1}(t) = \boldsymbol{F}(\boldsymbol{u}_{h_1}(t), \boldsymbol{z}_{h_1}(t)) \quad \forall t \in (0,T), \\ \boldsymbol{z}_{h_1}(0) = \boldsymbol{z}_{0,h_1}. \end{cases} \tag{31}$$

Activation model The Galerkin formulation related to the equation for γ_f reads: given $\boldsymbol{d}_{\boldsymbol{s},h_2} = \boldsymbol{d}_{\boldsymbol{s},h_2}(t)$ and $s_{h_2} = s_{h_2}(t) = \bar{\Pi}_{s_{h_1}}(\boldsymbol{x})$, find $\gamma_{f,h_2}(t) \in \mathcal{X}_{h_2}^r$ $\forall t \in (0,T)$ such that

$$\begin{aligned} &\int_{\Omega_0} \frac{\partial \gamma_{f,h_2}}{\partial t}\phi_i d\Omega_0 + \varepsilon \int_{\Omega_0} \frac{1}{g(s_{h_2})}\nabla\gamma_{f,h_2} \cdot \nabla\phi_i d\Omega_0 \\ &\qquad - \int_{\Omega_0} \frac{1}{g(s_{h_2})}\Phi(s_{h_2}, \gamma_{f,h_2}, \boldsymbol{d}_{\boldsymbol{s},h_2})\phi_i d\Omega_0 = 0 \quad \forall i = 1, ..., N_{\gamma_f}, \end{aligned} \tag{32}$$

with $\gamma_{f,h_2}(0) = \sum_{j=1}^{N_{\gamma_f}} (\gamma_{f,0}, \phi_j)_{L^2(\Omega_0)}\phi_j$ and $s_{h_2}(t)$ interpolation of $s_{h_1}(t)$ by means of RL-RBF, i.e. formula (5). By introducing the proper matrices, the following system of ODEs is obtained:

$$\begin{cases} \mathcal{M}\dot{\boldsymbol{\gamma}}_{f,h_2}(t) + \varepsilon\mathcal{K}(s_{h_2}(t))\boldsymbol{\gamma}_{f,h_2}(t) + \boldsymbol{\Phi}(s_{h_2}(t), \boldsymbol{\gamma}_{f,h_2}(t), \boldsymbol{d}_{\boldsymbol{s},h_2})(t)) = \boldsymbol{0} \quad \forall t \in (0,T), \\ \boldsymbol{\gamma}_{f,h_2}(0) = \boldsymbol{\gamma}_{f,0,h_2}. \end{cases} \tag{33}$$

Mechanical model We denote by $[\mathcal{X}_{h_2}^r]^3$ the finite dimensional subspace of vector valued functions and by $\{\boldsymbol{\phi}_i\}_{i=1}^{N_{\boldsymbol{d}_{\boldsymbol{s}}}}$ its basis. The semi-discretized version of (17) reads: given $\gamma_{f,h_2}(t)$, find $\boldsymbol{d}_{\boldsymbol{s},h_2} = \boldsymbol{d}_{\boldsymbol{s},h_2}(t) \in [\mathcal{X}_{h_2}^r]^3$ $\forall t \in (0,T)$ such that

$$\begin{aligned}
&\int_{\Omega_0} \rho_s \frac{\partial^2 \boldsymbol{d}_{\boldsymbol{s},h_2}}{\partial t^2} \cdot \boldsymbol{\phi}_i d\Omega_0 + \int_{\Omega_0} \boldsymbol{P}(\boldsymbol{d}_{\boldsymbol{s},h_2}, \gamma_{f,h_2}) : \nabla \boldsymbol{\phi}_i d\Omega_0 \\
&\quad + \int_{\Gamma_0^{epi}} \Bigg[(\boldsymbol{N} \otimes \boldsymbol{N}) \left(K_\perp^{epi} \boldsymbol{d}_{\boldsymbol{s},h_2} + C_\perp^{epi} \frac{\partial \boldsymbol{d}_{\boldsymbol{s},h_2}}{\partial t} \right) \\
&\quad + (\boldsymbol{I} - \boldsymbol{N} \otimes \boldsymbol{N}) \left(K_\parallel^{epi} \boldsymbol{d}_{\boldsymbol{s},h_2} + C_\parallel^{epi} \frac{\partial \boldsymbol{d}_{\boldsymbol{s},h_2}}{\partial t} \right) \Bigg] \cdot \boldsymbol{\phi}_i d\Gamma_0 \\
&\quad = - \int_{\Gamma_0^{endo}} p^{endo}(t) \boldsymbol{N} \cdot \boldsymbol{\phi}_i d\Gamma_0 \quad \forall i = 1, ..., N_{\boldsymbol{d_s}},
\end{aligned} \tag{34}$$

with $\boldsymbol{d}_{\boldsymbol{s},h_2}(0) = \sum_{j=1}^{N_{\boldsymbol{d_s}}} (\boldsymbol{d}_{\boldsymbol{s},\boldsymbol{0}}, \boldsymbol{\phi}_j)_{[L^2(\Omega_0)]^3} \boldsymbol{\phi}_j$, $\dot{\boldsymbol{d}}_{\boldsymbol{s},h_2}(0) = \sum_{j=1}^{N_{\boldsymbol{d_s}}} (\dot{\boldsymbol{d}}_{\boldsymbol{s},\boldsymbol{0}}, \boldsymbol{\phi}_j)_{[L^2(\Omega_0)]^3} \boldsymbol{\phi}_j$.

The algebraic formulation reads:

$$\begin{cases}
\rho_s \mathcal{M} \ddot{\boldsymbol{d}}_{\boldsymbol{s},h_2}(t) + \mathcal{F} \dot{\boldsymbol{d}}_{\boldsymbol{s},h_2}(t) + \mathcal{G} \boldsymbol{d}_{\boldsymbol{s},h_2}(t) + \boldsymbol{S}(\boldsymbol{d}_{\boldsymbol{s},h_2}(t), \boldsymbol{\gamma}_{f,h_2}(t)) = \boldsymbol{p}^{endo}(t) \quad \text{in } t \in (0,T), \\
\boldsymbol{d}_{\boldsymbol{s},h_2}(0) = \boldsymbol{d}_{\boldsymbol{s},\boldsymbol{0},h_2}, \quad \dot{\boldsymbol{d}}_{\boldsymbol{s},h_2}(0) = \dot{\boldsymbol{d}}_{\boldsymbol{s},\boldsymbol{0},h_2},
\end{cases} \tag{35}$$

with:

$$\boldsymbol{S}_i(\boldsymbol{d}_{\boldsymbol{s},h_2}(t), \boldsymbol{\gamma}_{f,h_2}(t)) = \int_{\Omega_0} \boldsymbol{P}(\boldsymbol{d}_{\boldsymbol{s},h_2}, \boldsymbol{\gamma}_{f,h_2}) : \nabla \boldsymbol{\phi}_i d\Omega_0,$$

$$\mathcal{F}_{i,j} = \int_{\Gamma_0^{epi}} \left[(\boldsymbol{N} \otimes \boldsymbol{N}) C_\perp^{epi} + (\boldsymbol{I} - \boldsymbol{N} \otimes \boldsymbol{N}) C_\parallel^{epi} \right] \boldsymbol{\phi}_j \cdot \boldsymbol{\phi}_i d\Gamma_0,$$

$$\mathcal{G}_{i,j} = \int_{\Gamma_0^{epi}} \left[(\boldsymbol{N} \otimes \boldsymbol{N}) K_\perp^{epi} + (\boldsymbol{I} - \boldsymbol{N} \otimes \boldsymbol{N}) K_\parallel^{epi} \right] \boldsymbol{\phi}_j \cdot \boldsymbol{\phi}_i d\Gamma_0.$$

Equations (27), (31), (32) and (34) provide the semi-discretization of (21) in a splitted fashion ready for a partitioned and staggered time discretization.

4.2.2 Time discretization

In order to fully discretize the electromechanical problem, we introduce a block vector $\boldsymbol{y} = \{\boldsymbol{y}_{\boldsymbol{z}}, \boldsymbol{y}_u, \boldsymbol{y}_{\gamma_f}, \boldsymbol{y}_{\boldsymbol{d_s}}\}$ containing all the unknowns of the problem and we reformulate the semi-discrete problem as follows:

$$\begin{cases}
\dfrac{d\boldsymbol{y}_{\boldsymbol{z}}(t)}{dt} + \mathcal{T}_{\boldsymbol{y}_{\boldsymbol{z}}}(\boldsymbol{y}(t)) = \boldsymbol{H}_{\boldsymbol{y}_{\boldsymbol{z}}}(t) & \forall t \in (0,T), \\
\mathcal{M} \dfrac{d\boldsymbol{y}_u(t)}{dt} + \mathcal{T}_{\boldsymbol{y}_u}(\boldsymbol{y}(t)) = \boldsymbol{H}_{\boldsymbol{y}_u}(t) & \forall t \in (0,T), \\
\mathcal{M} \dfrac{d\boldsymbol{y}_{\gamma_f}(t)}{dt} + \mathcal{T}_{\boldsymbol{y}_{\gamma_f}}(\boldsymbol{y}(t)) = \boldsymbol{H}_{\boldsymbol{y}_{\gamma_f}}(t) & \forall t \in (0,T), \\
\rho_s \mathcal{M} \dfrac{d^2 \boldsymbol{y}_{\boldsymbol{d_s}}(t)}{dt^2} + \mathcal{T}_{\boldsymbol{y}_{\boldsymbol{d_s}}}(\boldsymbol{y}(t)) = \boldsymbol{H}_{\boldsymbol{y}_{\boldsymbol{d_s}}}(t) & \forall t \in (0,T), \\
\boldsymbol{y}_{\boldsymbol{z}}(0) = \boldsymbol{y}_{\boldsymbol{z},\boldsymbol{0}}, \\
\boldsymbol{y}_u(0) = \boldsymbol{y}_{u,0}, \\
\boldsymbol{y}_{\gamma_f}(0) = \boldsymbol{y}_{\gamma_f,0}, \\
\boldsymbol{y}_{\boldsymbol{d_s}}(0) = \boldsymbol{y}_{\boldsymbol{d_s},\boldsymbol{0}}, \\
\dot{\boldsymbol{y}}_{\boldsymbol{d_s}}(0) = \boldsymbol{0},
\end{cases} \tag{36}$$

where $\mathcal{T}$ and $\boldsymbol{H}$ terms represent the core models. The time discretization performed with the BDF scheme of general order σ [60] reads as follows:

$$
\begin{aligned}
\frac{d\boldsymbol{y}_{\boldsymbol{z}}(t^{n+1})}{dt} &\approx \frac{1}{\Delta t}\left(\theta_0^I \boldsymbol{y}_{\boldsymbol{z}}^{n+1} - \boldsymbol{y}_{\boldsymbol{z}}^I\right), \quad \boldsymbol{y}_{\boldsymbol{z}}^I = \sum_{k=1}^{\sigma} \theta_k^I \boldsymbol{y}_{\boldsymbol{z}}{}^{n-k+1}, \\
\frac{d\boldsymbol{y}_u(t^{n+1})}{dt} &\approx \frac{1}{\Delta t}\left(\theta_0^I \boldsymbol{y}_u^{n+1} - \boldsymbol{y}_u^I\right), \quad \boldsymbol{y}_u^I = \sum_{k=1}^{\sigma} \theta_k^I \boldsymbol{y}_u^{n-k+1}, \\
\frac{d\boldsymbol{y}_{\gamma_f}(t^{n+1})}{dt} &\approx \frac{1}{\Delta t}\left(\theta_0^I \boldsymbol{y}_{\gamma_f}^{n+1} - \boldsymbol{y}_{\gamma_f}^I\right), \quad \boldsymbol{y}_{\gamma_f}^I = \sum_{k=1}^{\sigma} \theta_k^I \boldsymbol{y}_{\gamma_f}^{n-k+1}, \\
\frac{d^2\boldsymbol{y}_{\boldsymbol{d_s}}(t^{n+1})}{dt^2} &\approx \frac{1}{(\Delta t)^2}\left(\theta_0^{II} \boldsymbol{y}_{\boldsymbol{d_s}}^{n+1} - \boldsymbol{y}_{\boldsymbol{d_s}}^{II}\right), \quad \boldsymbol{y}_{\boldsymbol{d_s}}^{II} = \sum_{k=1}^{\sigma+1} \theta_k^{II} \boldsymbol{y}_{\boldsymbol{d_s}}^{n-k+1},
\end{aligned}
\tag{37}
$$

where $\Delta t = \dfrac{T}{N_T}$ is the timestep, N_T is the total number of timesteps, and θ_k^I, θ_k^{II}, $k = 0, ..., \sigma/\sigma + 1$ depend on the order of the BDF scheme. We use $\sigma = 1$.

4.2.3 Segregated scheme

Implicit monolithic strategies are stable and lead to accurate results, as shown in [33]. However there are two types of drawbacks connected with this approach. We are forced to use the same timestep for both electrical and mechanical parts even if the timescale of electrophysiological phenomena is much smaller than the one of the myocardial activation/mechanics. Moreover the calculation of the Jacobian matrix $\mathcal{J}_{EM}$ is quite demanding and this matrix requires a significant amount of RAM. In order to overcome these issues, we propose a segregated strategy based on the Godunov splitting scheme [35]. This approach permits to advance in time faster and consuming less memory, at the expense of introducing first order error on the solution [32, 34]. However, due to the fact that partitioned schemes do not guarantee unconditional stability in general [13], we have to be careful in the choice of both timestep and number of elements for each mesh. For both electrophysiology and activation we employ, as done in [32], a semi-implicit scheme. Mechanics is instead numerically discretized in time implicitly, due to the fact that the highly non-linear (exponential) terms of the strain energy function $\mathcal{W}$ would need a restrictive Δt in both the semi-implicit and explicit contexts. We refer from now on to $(\mathcal{I}_{\mathcal{SI}}) - (\mathcal{E}_{\mathcal{SI}}) - (\mathcal{A}_{\mathcal{SI}})$ for the fully-segregated-semi-implicit scheme applied to the ionic, monodomain and activation models, and to $\mathcal{M}_{\mathcal{I}}$ for the implicit scheme applied to the mechanical core. We employ a staggered approach in which two different timesteps are used for $(\mathcal{I}_{\mathcal{SI}}) - (\mathcal{E}_{\mathcal{SI}})$ and $(\mathcal{A}_{\mathcal{SI}}) - (\mathcal{M}_{\mathcal{I}})$. We define Δt the timestep for both activation and mechanics. $\tau = \frac{\Delta t}{N_{sub}}$ is the timestep for electrophysiology (ionic and monodomain models), with $N_{sub} \in \mathbb{N}$ number of intermediate substeps that must be done by $(\mathcal{I}_{\mathcal{SI}}) - (\mathcal{E}_{\mathcal{SI}})$ before a timestep Δt of $(\mathcal{A}_{\mathcal{SI}}) - (\mathcal{M}_{\mathcal{I}})$ is performed. The time advancement that has been just described is sketched in Figure 7.

We set $t^{n+\frac{m}{N_{sub}}} = t^n + m\tau$ for $m = 1, ..., N_{sub}$.

Problem $(\mathcal{I}_{\mathcal{SI}}) - (\mathcal{E}_{\mathcal{SI}})$ from t^n to t^{n+1} reads:

- Find $\bar{\boldsymbol{z}}_{h_1}^{n+\frac{m}{N_{sub}}}$ defined on $\mathcal{T}_{h_1}$ by solving:

$$
\frac{\theta_0^I}{\tau} \bar{\boldsymbol{z}}_{h_1}^{n+\frac{m}{N_{sub}}} = \frac{1}{\tau} \bar{\boldsymbol{z}}_{h_1}^I + \boldsymbol{F}(\bar{\boldsymbol{u}}_{h_1}^*, \bar{\boldsymbol{z}}_{h_1}^*).
\tag{38}
$$

- Interpolate $\bar{\boldsymbol{d}}_{\boldsymbol{s},h_2}^*$ on the fine mesh $\mathcal{T}_{h_1}$ only one time, at $t = t^n$. Use $\bar{\boldsymbol{z}}_{h_1}^{n+\frac{m}{N_{sub}}}$ from (38) and $\bar{\boldsymbol{d}}_{\boldsymbol{s},h_1}^*$ to find $\bar{\boldsymbol{u}}_{h_1}^{n+\frac{m}{N_{sub}}}$ defined on $\mathcal{T}_{h_1}$ by solving:

$$
\begin{aligned}
\left(\frac{\theta_0^I}{\tau}\mathcal{M} + \mathcal{K}(\bar{\boldsymbol{d}}_{\boldsymbol{s},h_1}^*) + \mathcal{I}_u^{ion}(\bar{\boldsymbol{u}}_{h_1}^*, \bar{\boldsymbol{z}}_{h_1}^{n+\frac{m}{N_{sub}}})\right) \bar{\boldsymbol{u}}_{h_1}^{n+\frac{m}{N_{sub}}} &= \frac{1}{\tau}\mathcal{M}\bar{\boldsymbol{u}}_{h_1}^I + \\
\tilde{\mathcal{I}}^{ion}(\bar{\boldsymbol{u}}_{h_1}^*, \bar{\boldsymbol{z}}_{h_1}^{n+\frac{m}{N_{sub}}}) - \mathcal{I}_{\boldsymbol{z}}^{ion}(\bar{\boldsymbol{u}}_{h_1}^*, \bar{\boldsymbol{z}}_{h_1}^{n+\frac{m}{N_{sub}}})\bar{\boldsymbol{z}}_{h_1}^{n+\frac{m}{N_{sub}}} &+ \mathcal{M}\mathcal{I}^{app}(t^{n+\frac{m}{N_{sub}}}),
\end{aligned}
\tag{39}
$$

for $m = 1, ..., N_{sub}$, where $\bar{\boldsymbol{u}}_{h_1}^I, \bar{\boldsymbol{z}}_{h_1}^I$ are evaluated by using the variables on the fine mesh $\mathcal{T}_{h_1}$ at times $t^n, t^n - \tau, ..., t^n - (\sigma - 1)\tau$, with $\sigma = 1$ in our case. After solving (38) and (39) for N_{sub} steps, treat $(\mathcal{A}_{\mathcal{SI}}) - (\mathcal{M}_{\mathcal{I}})$ at t^{n+1} in the following way:

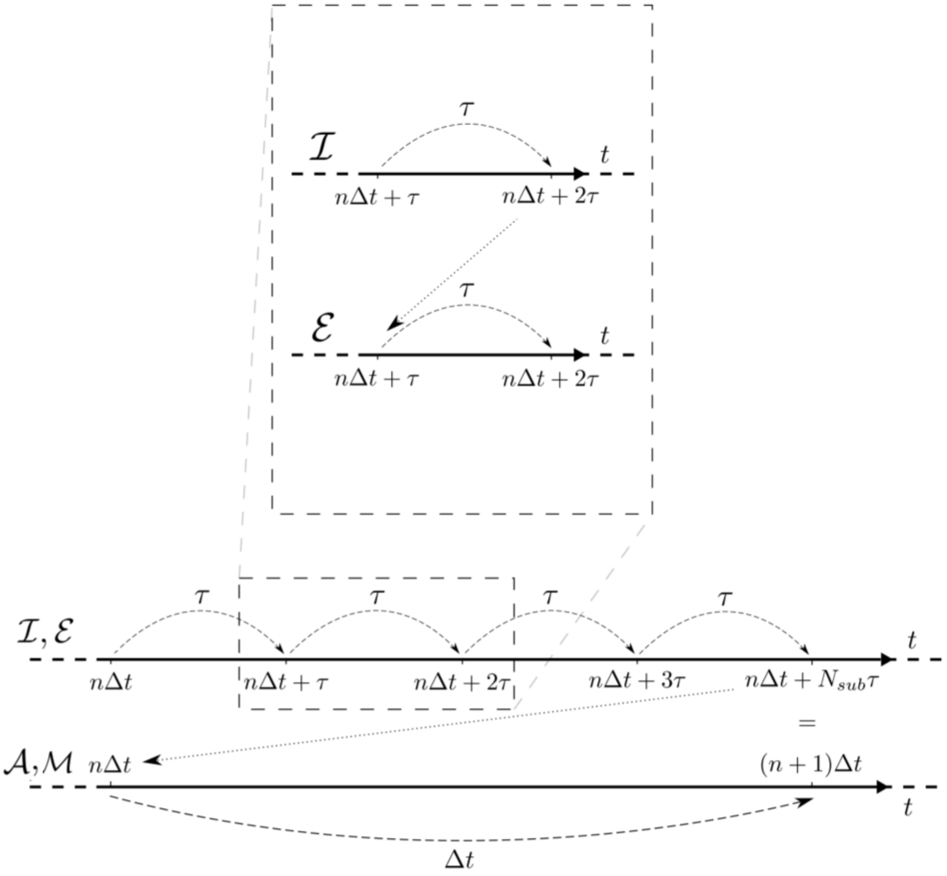

Figure 7: Time advancement for $(\mathcal{I}_{\mathcal{SI}}) - (\mathcal{E}_{\mathcal{SI}}) - (\mathcal{A}_{\mathcal{SI}}) - (\mathcal{M}_{\mathcal{I}})$ scheme

- Interpolate $\bar{\boldsymbol{z}}_{h_1}^{n+1}$ from (38) on the coarse mesh $\mathcal{T}_{h_2}$, and use $\bar{\boldsymbol{z}}_{h_2}^{n+1}$ to find $\bar{\gamma}_{\boldsymbol{f},h_2}^{n+1}$ by solving:

$$\begin{aligned}&\left(\frac{\theta_0^I}{\tau}\mathcal{M} + \varepsilon\mathcal{K}(\bar{\boldsymbol{z}}_{h_2}^{n+1}) + \mathcal{P}_{\gamma_f}(\bar{\gamma}_{\boldsymbol{f},h_2}^{*}, \bar{\boldsymbol{d}}_{\boldsymbol{s},h_2}^{*}, \bar{\boldsymbol{z}}_{h_2}^{n+1})\right)\bar{\gamma}_{\boldsymbol{f},h_2}^{n+1}\\ &= \frac{1}{\tau}\mathcal{M}\bar{\gamma}_{\boldsymbol{f},h_2}^{I} + \tilde{\boldsymbol{\Phi}}(\bar{\gamma}_{\boldsymbol{f},h_2}^{*}, \bar{\boldsymbol{d}}_{\boldsymbol{s},h_2}^{*}, \bar{\boldsymbol{z}}_{h_2}^{n+1}).\end{aligned} \tag{40}$$

- Finally, $\bar{\boldsymbol{d}}_{\boldsymbol{s},h_2}^{n+1}$ is obtained by solving:

$$\begin{aligned}&\left(\rho_s\frac{\theta_0^{II}}{(\Delta t)^2}\mathcal{M} + \frac{\theta_0^{'}}{\Delta t}\mathcal{F} + \mathcal{G}\right)\bar{\boldsymbol{d}}_{\boldsymbol{s},h_2}^{n+1} + \boldsymbol{S}(\bar{\boldsymbol{d}}_{\boldsymbol{s},h_2}^{n+1}, \bar{\gamma}_{\boldsymbol{f},h_2}^{n+1})\\ &= \rho_s\frac{1}{(\Delta t)^2}\mathbb{M}\bar{\boldsymbol{d}}_{\boldsymbol{s},h_2}^{II} + \frac{1}{\Delta t}\mathbb{F}\bar{\boldsymbol{d}}_{\boldsymbol{s},h_2}^{I} + \boldsymbol{p}^{endo}(t^{n+1}) - \boldsymbol{S}_{\boldsymbol{0}},\end{aligned} \tag{41}$$

  by means of the Newton method [60]. $\bar{\gamma}_{\boldsymbol{f},h_2}^{I}$, $\bar{\boldsymbol{d}}_{\boldsymbol{s},h_2}^{I}$ and $\bar{\boldsymbol{d}}_{\boldsymbol{s},h_2}^{II}$ are evaluated by using the variables on the coarse mesh $\mathcal{T}_{h_2}$ at previous timesteps.

$\bar{\boldsymbol{z}}_{h_1}^{*}, \bar{\boldsymbol{u}}_{h_1}^{*}, \bar{\gamma}_{\boldsymbol{f},h_2}^{*}$, $\bar{\boldsymbol{d}}_{\boldsymbol{s},h_1}^{*}$ and $\bar{\boldsymbol{d}}_{\boldsymbol{s},h_2}^{*}$ are extrapolations of all variables of the model using Newton-Gregory backward polynomials [14].

4.3 Numerical results

In this subsection we present a numerical simulation of a full heartbeat lasting 0.8 s in the electromechanical framework, by considering an idealized left ventricle in physiological conditions. We use LifeV [45], an open-source

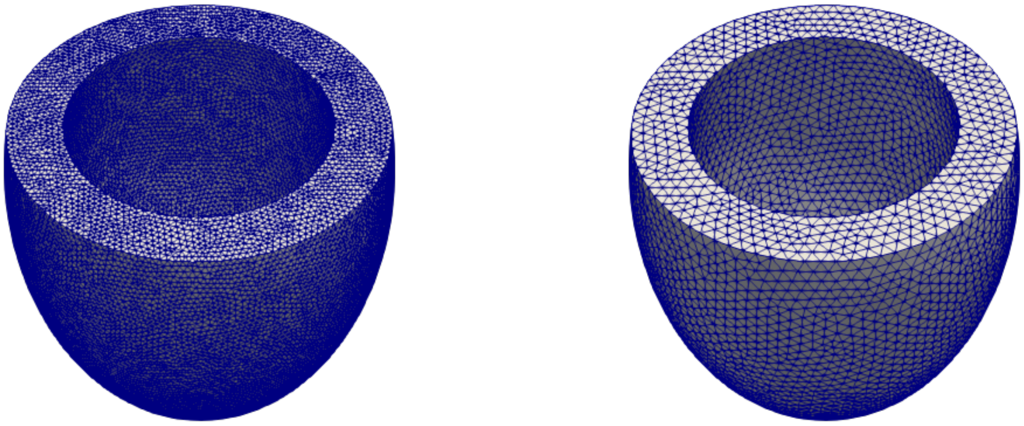

Figure 8: View from above of the prolate ellipsoidal meshes for electrophysiology (left), activation and mechanics (right)

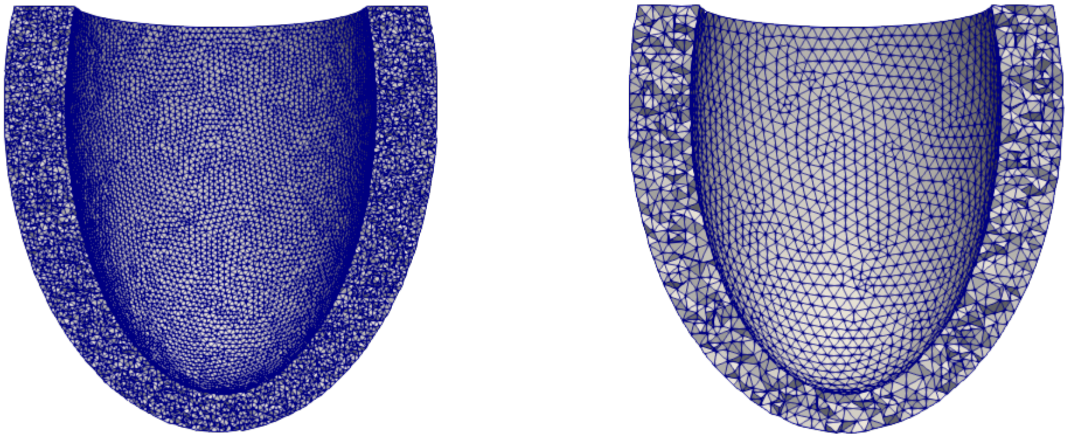

Figure 9: Cut front view of the prolate ellipsoidal meshes for electrophysiology (left) and activation+mechanics (right).

finite element library, for the resolution of the electromechanical problem in a High Performance Computing framework and for the implementation of the numerical method. All the computations were carried out using a full node (32 Intel® Xeon® E5-4610 v2 2.3GHz cores) of the HPC centre available at MOX.

Physics/Fields	Number of elements	Number of vertices	h_{mean}
Electrophysiology	1’002’886	170’009	1.2 mm
Activation and mechanics	119’419	21’928	3 mm

Table 2: Information about the two meshes of the idealized left ventricle with the corresponding number of elements, number of vertices and average edge length.

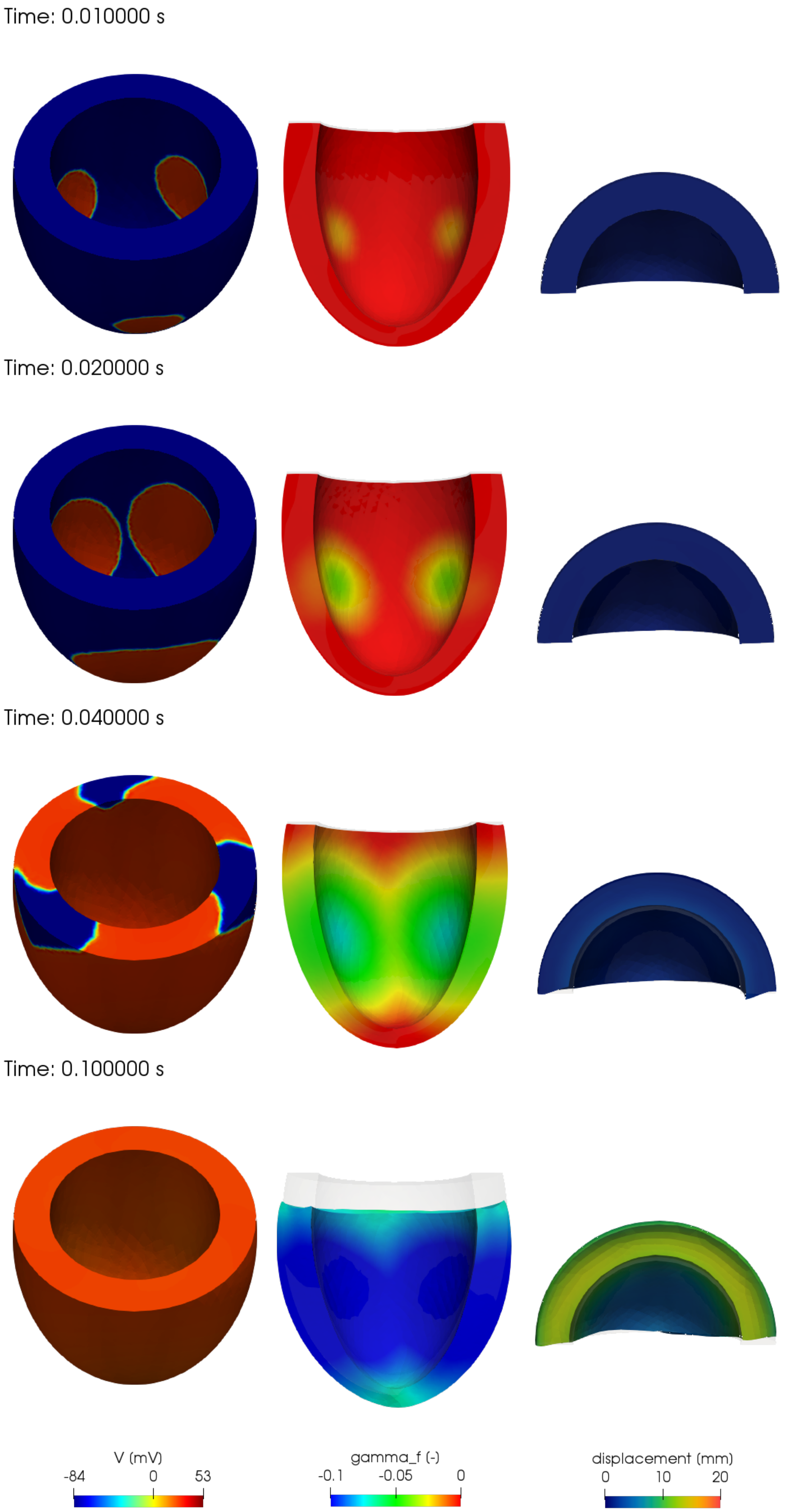

Figure 10: Evolution of transmembrane potential $V = 85.7u - 84$, γ_f and $\boldsymbol{d_s}$ in the idealized left ventricle over the time. The second and the third views of each picture are warped by the displacement magnitude.

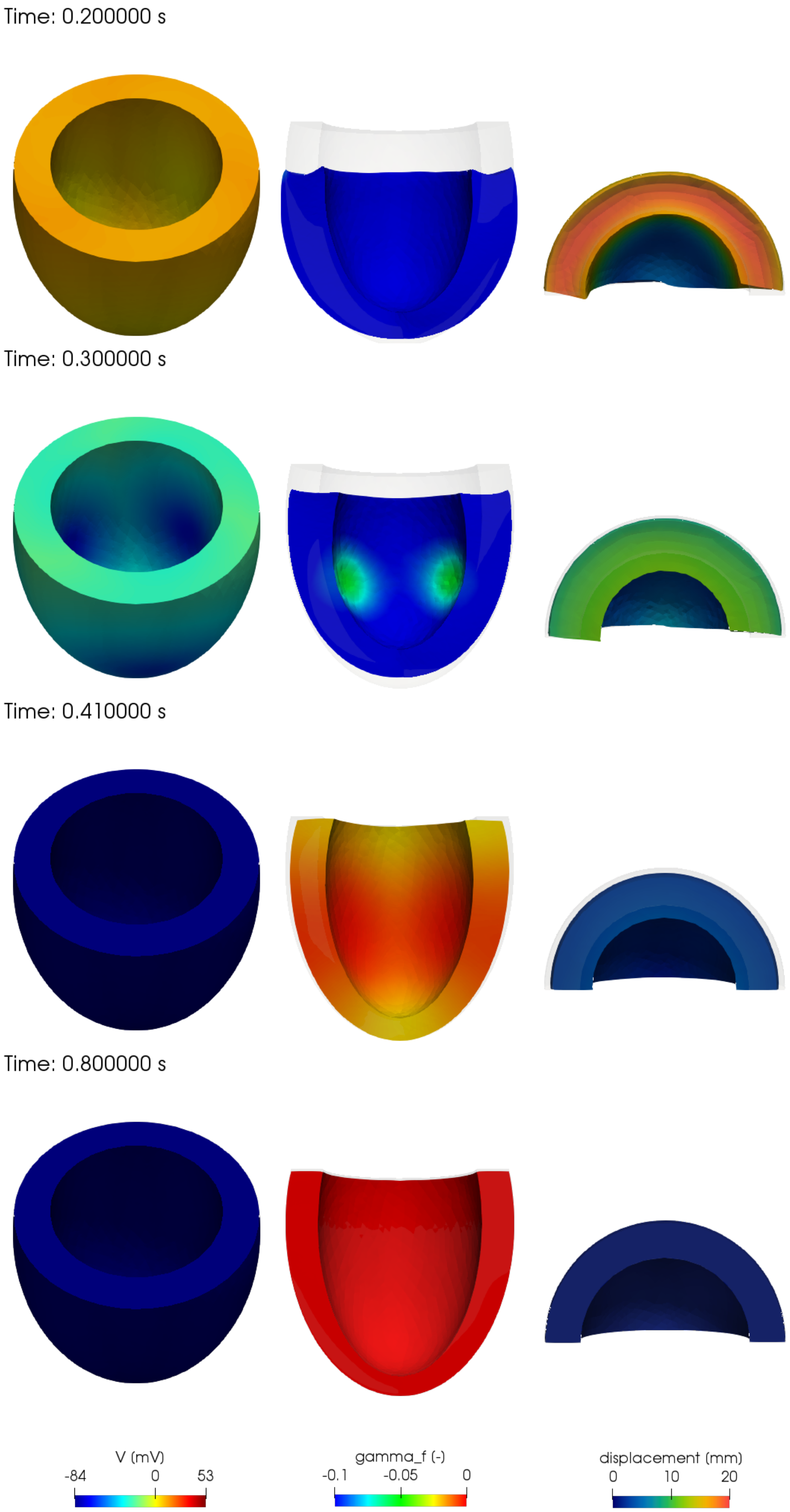

Figure 11: Evolution of transmembrane potential $V = 85.7u - 84$, γ_f and $\boldsymbol{d_s}$ in the idealized left ventricle over the time. The second and the third views of each picture are warped by the displacement magnitude.

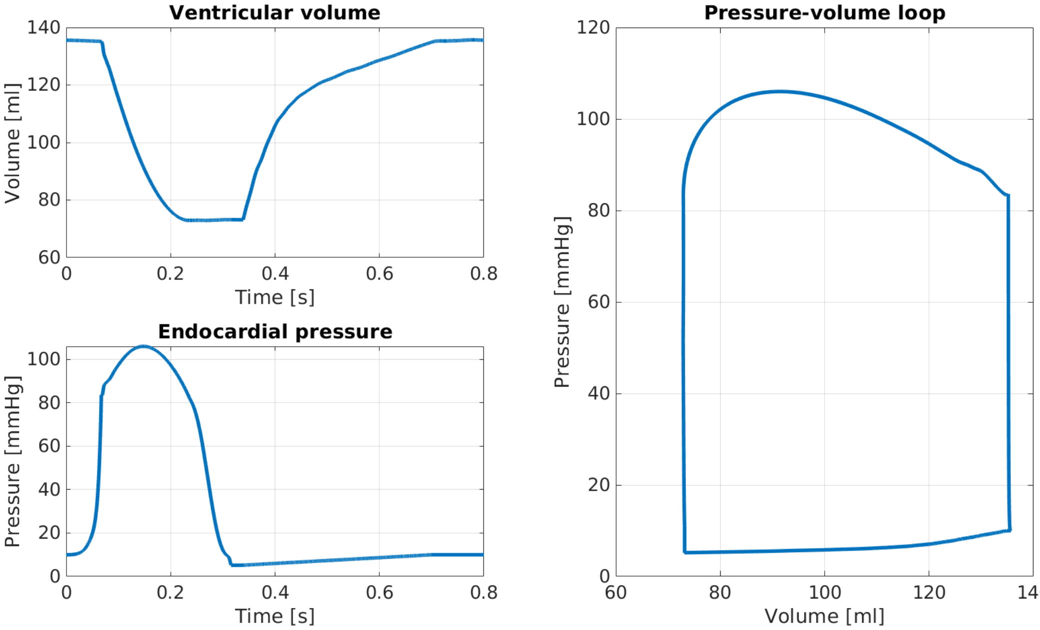

Figure 12: Ventricular volume and endocardial pressure over time (left) with pV-loop (right), for the idealized left ventricle.

In Figures 8 and 9 we show the meshes that we have used. They have been generated using VMTK - the Vascular Modelling Toolkit [4, 82], and their information are reported in Table 2. With VMTK we can choose a certain diameter h_{mean} and we can generate fine enough meshes featuring elements with similar aspect ratio. This toolkit is also used for the tagging procedure to determine which elements belong to the base, the endocardium and the epicardium. Different tags are assigned to these three different regions of the computational domain to apply in a proper way boundary conditions. With our methodology we are also able to deal with different grids that are completely independent. We use $\mathcal{P}^1$ finite elements in order to approximate monodomain, activation and mechanics equations, so that the unknowns are actually calculated on the vertices of each tetrahedron. The ionic model evolves directly on the vertices of each element. We employ a first order BDF scheme in time [60]. The timestep for electrophysiology is $\Delta t = 50\ \mu s$, whereas the one for activation and mechanics is $\Delta t = 250\ \mu s$. We also have to solve several linear systems coming from:

- Interpolation of the gating variable s from the coarse mesh to the fine mesh;
- Interpolation of the displacement $\boldsymbol{d_s}$ from the fine mesh to the coarse mesh;
- $(\mathcal{I}_{\mathcal{SI}})$ evolution in time with a small timestep;
- $(\mathcal{E}_{\mathcal{SI}})$ evolution in space and time with a small timestep;
- $(\mathcal{A}_{\mathcal{SI}})$ evolution in space and time with a larger timestep;
- $(\mathcal{M}_{\mathcal{I}})$ evolution in space and time with a larger timestep (inversion of the jacobian matrix at each Newton iteration).

We perform these tasks using the GMRES method with a stopping criterion based on the relative residual and a tolerance given by 10^{-8}. We apply a current I_{app} (term of the monodomain model) for $2\ ms$ in three different points of the myocardium to trigger the electrical signal in the left ventricle. Even if we do not keep into account precisely the propagation of stimuli inside the Purkinje network [65, 86], the electrical activation of the tissue that we propose is known to provide physically acceptable results [32].

In literature there are several rule-based techniques to generate fibers and sheets distribution [8, 24, 67] for both idealized and patient-specific cases. We use the strategy proposed in [33], where fibers rotate transmurally from the epicardium, with $\alpha_{epi} = -60°$ to the endocardium, with $\alpha_{endo} = +60°$. In order to properly take into account the internal stresses of the myocardium at the beginning of the electromechanical simulation, we have to apply the so called prestress to our computational domain. We compute a distribution of stresses such that the reference geometry is in equilibrium with the blood pressure p^{endo} at the end of the diastolic phase. An additive decomposition of the strain

σ_t	σ_l	λ_{epi}	λ_{endo}	$\bar{k}_{epi}$	$\bar{k}_{endo}$	$\bar{k}^{'}$	α	c_0	$\hat{\mu}_A^1$	$\hat{\mu}_A^2$	$\hat{\mu}_A^3$
17.61	120.4	0.8	0.5	0.75	1.0	-7.0	-6.0	0.05	2.1	7.0	12
$\hat{\mu}_A^4$	ρ	B	$K_{\perp}^{epi}$	$K_{\parallel}^{epi}$	$C_{\perp}^{epi}$	$C_{\parallel}^{epi}$	C_p^I	C_p^{II}	C	R	
500	10^{-3}	50000	0.2	0.0	0.005	0.0	-5e-7	-5e-7	4500	3.5e-5	

Table 3: Parameters used in the electromechanical model: transversal and longitudinal conductivities $\left(\dfrac{mm^2}{s}\right)$; transmurally heterogeneous wall thickening coefficients λ_{epi}, λ_{endo}, $\bar{k}_{epi}$, $\bar{k}_{endo}$ and $\bar{k}^{'}$; activation model coefficients α $\left(\mu M^{-2}\right)$, c_0, and $\hat{\mu}_A$ $\left(\mu M^2 \cdot s\right)$ of the four cardiac phases expressed; density ρ $\left(\dfrac{g}{mm^3}\right)$; bulk modulus B (Pa); Robin boundary condition coefficients $\left(\dfrac{kPa}{mm}, \dfrac{kPa \cdot s}{mm}\right)$; relaxation parameters for the two isochoric phases C_p^I and C_p^{II} $\left(\dfrac{kPa \cdot s}{mm^3}\right)$; Windkessel model parameters C and R $\left(\dfrac{mm^3}{kPa}, \dfrac{kPa \cdot s}{mm^3}\right)$.

tensor $\hat{\boldsymbol{P}} = \boldsymbol{P}(\boldsymbol{d_s}) + \boldsymbol{P_0}$ is operated, where the prestress tensor $\boldsymbol{P_0}$ is determine to ensure a null displacement $\boldsymbol{d_{s,0}}$ in correspondance of the initial pressure at the endocardium. For more information about this technique we refer to [32, 33, 34].

In Figures 10 and 11 we observe the evolution in space and time of the transmembrane potential V, activation variable γ_f and displacement $\boldsymbol{d_s}$ over one entire heartbeat. The conduction velocity is overestimated due to the fact that, even if the electrophysiological mesh is fine, we should use a smaller value of h_{mean} to describe properly all the space scales and to have a convergent velocity of the wavefront [9, 33, 66]. The activation is slightly delayed with respect to the propagation of the action potential because it is driven by the calcium concentration (here approximated with the gating variable s), that evolves in time more slowly than the transmembrane potential. The myocardial tissue undergoes a significant thickening, which is in accordance with experimental observations [63]. A high value of the bulk modulus B permits to obtain a significant torsion of the left ventricle and to impose the quasi-incompressibility constraint. With the choice of parameters for the Robin boundary condition at the epicardium in the mechanics problem (17), we are able to properly keep into account the effect of the pericardium [57]: in this way we can reduce the movement of the apex and increase the contraction of the base.

The pV-loop is reported in Figure 12. Even if a comparison with in-vivo measurements would be meaningless, due to the fact that we are dealing with an idealized framework, we can say that the pV-loop developed over the simulation is in accordance with those observed experimentally [69] both from the qualitative and quantitative perspective. Moreover, both the range in pressure and volume during the systolic and the diastolic phases correspond to the physiological one of average individuals [72].

Finally, with reference to [33], we have also performed this simulation in a monolithic fashion. In this case we are forced to use the timestep Δt of electrophysiology also for both activation and mechanics, due to the fact that action potential and calcium dynamics need a higher resolution in time. For what concerns space discretization, we are again forced to use only the mesh of electrophysiology, even if we do not need such a high number of elements for the mechanical problem. For these reasons monolithic schemes are poorer in terms of performances with respect to segregated ones. With the approach presented in this paper we observe a 10x speed-up in the final computational time with respect to [33], describing also in a proper and accurate way both the time and space scales of this multiphysics problem.

5 Conclusions

In this work, we propose a novel segregated solver, which makes use of an accurate and efficient intergrid transfer operator based on radial basis functions to simulate the electromechanical activity of an idealized left ventricle. We consider a coupling between the monodomain equation and the Bueno-Orovio minimal ionic model for the electric part. Cardiac mechanics is modelled in the active strain formulation using the Holzapfel-Ogden constitutive law and a transmurally variable activation. Electrophysiology and mechanics are linked by means of a phenomenological model that reproduces fibers contraction. Prestress and additional 0D problems for the fluid permit to keep into account the interaction of the myocardium with the blood inside the left ventricle. We solve this multifield coupled problem in the High Performance Computing framework. The use of two different meshes is motivated by the fact that the level of resolution required by the two physics is not the same, going from an element size with the order of 0.1 mm for electrophysiology, to $1\ mm$ for mechanics. This allows to obtain a significant speed-up in the numerical simulation with respect to the case in which we use one single mesh that could be forced to have the fine resolution of the electric part. The same considerations lead to the choice of different timesteps and to solve the electromechanical problem in a staggered fashion, which is again faster and less memory-demanding in comparison with the monolithic approach.

6 Acknowledgements

This research is funded by the ERC Advanced Grant iHEART, "An Integrated Heart Model for the simulation of the cardiac function", 2017-2022, P.I.A. Quarteroni (ERC-2016-ADG, project ID: 740132). We sincerely thank Dr. A. Gerbi, Dr. M. Fedele, Dr. P. Africa, F. Regazzoni, and N. Barnafi for the useful discussions and their help with the use of the LifeV library.

References

[1] R. R. Aliev and A. V. Panfilov. "A simple two-variable model of cardiac excitation". In: *Chaos, Solitons & Fractals* 7 (1996), pp. 293–301.

[2] D. Ambrosi and S. Pezzuto. "Active stress vs. active strain in mechanobiology: constitutive issues". In: *Journal of Elasticity* 107 (2012), pp. 199–212.

[3] D. Ambrosi et al. "Electromechanical coupling in cardiac dynamics: the active strain approach". In: *SIAM Journal on Applied Mathematics* 71 (2011), pp. 605–621.

[4] L. Antiga et al. "An image-based modeling framework for patient-specific computational hemodynamics". In: *Medical and Biological Engineering and Computing* 46 (2008), pp. 1097–1112.

[5] C. M. Augustin et al. "Anatomically accurate high resolution modeling of human whole heart electromechanics: a strongly scalable algebraic multigrid solver method for nonlinear deformation". In: *Journal of Computational Physics* 305 (2016), pp. 622–646.

[6] B. Baillargeon et al. "The living heart project: a robust and integrative simulator for human heart function". In: *European Journal of Mechanics - A/Solids* 48 (2014), pp. 38–47.

[7] L. Barbarotta et al. "A transmurally heterogeneous orthotropic activation model for ventricular contraction and its numerical validation". In: *Numerical Methods in Biomedical Engineering* 34 (2018).

[8] J. D. Bayer et al. "A novel rule-based algorithm for assigning myocardial fiber orientation to computational heart models". In: *Annals of Biomedical Engineering* 40 (2012), pp. 2243–2254.

[9] M. Bendahmane, R. Bürger, and R. Ruiz-Baier. "A finite volume scheme for cardiac propagation in media with isotropic conductivities". In: *Mathematics and Computers in Simulation* 80 (2010), pp. 1821–1840.

[10] A. Bueno-Orovio, E. M. Cherry, and F. H. Fenton. "Minimal model for human ventricular action potentials in tissue". In: *Journal of Theoretical Biology* 253 (2008), pp. 544–560.

[11] M. D. Buhmann. *Radial Basis Functions: Theory and Implementations*. Cambridge University Press, 2003.

[12] E. Burman and A. Ern. "The discrete maximum principle for stabilized finite element methods". In: *Numerical Mathematics and Advanced Applications*. Springer, 2003, pp. 557–566.

[13] P. Causin, J. F. Gerbeau, and F. Nobile. "Added-mass effect in the design of partitioned algorithms for fluid-structure problems". In: *Computer Methods in Applied Mechanics and Engineering* 194 (2005), pp. 4506–4527.

[14] F. E. Cellier and E. Kofman. *Continuous System Simulation*. Springer, 2006.

[15] R. Chabiniok et al. "Multiphysics and multiscale modelling, data-model fusion and integration of organ physiology in the clinic: ventricular cardiac mechanics". In: *Interface Focus* 6 (2016), pp. 15–83.

[16] D. Chapelle et al. "Numerical simulation of the electromechanical activity of the heart". In: *International Conference on Functional Imaging and Modeling of Heart* 5528 (2009), pp. 357–365.

[17] X. Chen. "The analysis of intergrid transfer operators and multigrid methods for nonconforming finite elements". In: *Electronic Transactions on Numerical Analysis* 6 (1997), pp. 78–96.

[18] A. Cheng et al. "Transmural cardiac strains in the lateral wall of the ovine left ventricle". In: *American Journal of Physiology. Heart and Circulatory Physiology* 288 (2005), pp. 1546–1556.

[19] P. Colli Franzone, L. F. Pavarino, and G. Savaré. "Computational electrocardiology: mathematical and numerical modeling". In: *Complex systems in Biomedicine*. Springer, 2006, pp. 187–241.

[20] P. Colli Franzone, L. F. Pavarino, and S. Scacchi. *Mathematical Cardiac Electrophysiology*. Springer, 2014.

[21] F. S. Costabal et al. "The importance of mechano-electrical feedback and inertia in cardiac electromechanics". In: *Computer Methods in Applied Mechanics and Engineering* 320 (2017), pp. 352–368.

[22] S. Deparis, D. Forti, and A. Quarteroni. *A rescaled localized radial basis functions interpolation on non-cartesian and non-conforming grids*. MATHICSE Technical Report. EPFL, 2013.

[23] S. Doll and K. Schweizerhof. "On the development of volumetric strain energy functions". In: *Journal of Applied Mathematics* 67 (2000), pp. 17–21.

[24] R. Doste, D. Soto-Iglesias, and G. Bernardino. "A rule-based method to model myocardial fiber orientation in cardiac biventricular geometries with outflow tracts". In: *Numerical Methods in Biomedical Engineering* 35 (2019).

[25] P. Duchon. "Splines minimizing rotation invariant semi-norms in sobolev spaces". In: (1977), pp. 85–100.

[26] T. S. E. Eriksson et al. "Influence of myocardial fiber/sheet orientations on left ventricular mechanical contraction". In: *Mathematics and Mechanics of Solids* 18 (2013), pp. 592–606.

[27] M. Fedele, E. Faggiano, and A. Quarteroni. "A patient-specific aortic valve model based on moving resistive immersed implicit surfaces". In: *Biomechanics and Modeling in Mechanobiology* 16 (2017), pp. 1779–1803.

[28] L. Formaggia, A. Quarteroni, and A. Veneziani. *Cardiovascular Mathematics: Modeling and Simulation of the Circulatory System*. Springer Science & Business Media, 2010.

[29] D. Forti and L. Dede'. "Semi-implicit BDF time discretization of the Navier-Stokes equations with VMS-LES modeling in a High Performance Computing framework". In: *Computers & Fluids* 117 (2015), pp. 168–182.

[30] C. Franke and R. Schaback. "Solving partial differential equations by collocation using radial basis functions". In: *Applied Mathematics and Computation* 93 (1998), pp. 73–82.

[31] J. A. S. Freeman and D. Saad. "Learning and generalisation in radial basis function networks". In: *Neural computation* 7 (1995), pp. 1000–1020.

[32] A. Gerbi. "Numerical approximation of cardiac electro-fluid-mechanical models: coupling strategies for large-scale simulation". PhD thesis. EPFL, 2018.

[33] A. Gerbi, L. Dede', and A. Quarteroni. "A monolithic algorithm for the simulation of cardiac electromechanics in the human left ventricle". In: *Mathematics in Engineering* 1 (2018), pp. 1–37.

[34] A. Gerbi, L. Dede', and A. Quarteroni. *Segregated algorithms for the numerical simulation of cardiac electromechanics in the left human ventricle*. MOX Report. Politecnico di Milano, 2018.

[35] S. Godunov. "A difference method for numerical calculation of discontinuous solutions of the equations of hydrodynamics". In: *Matematicheskii Sbornik* 89 (1959), pp. 271–306.

[36] S. Göktepe and E. Kuhl. "Electromechanics of the heart: a unified approach to the strongly coupled excitation-contraction problem". In: *Computational Mechanics* 45 (2010), pp. 227–243.

[37] A. M. Gordon, A. F. Huxley, and F. J. Julian. "The variation in isometric tension with sarcomere length in vertebrate muscle fibres". In: *The Journal of Physiology* 184 (1966), pp. 170–192.

[38] J. M. Guccione and A. D. McCulloch. "Finite element modeling of ventricular mechanics". In: *Theory of Heart*. Springer, 1991, pp. 121–144.

[39] J. M. Guccione, A. D. McCulloch, and L. K. Waldman. "Passive material properties of intact ventricular myocardium determined from a cylindrical model". In: *Journal of Biomechanical Engineering* 113 (1991), pp. 42–55.

[40] G. A. Holzapfel and R. W. Ogden. "Constitutive modelling of passive myocardium: a structurally based framework for material characterization". In: *Mathematical, Physical and Engineering Sciences* 367 (2009), pp. 3445–3475.

[41] M. C. Hsu and Y. Bazilevs. "Blood vessel tissue prestress modeling for vascular fluid-structure interaction simulation". In: *Finite Elements in Analysis and Design* 47 (2011), pp. 593–599.

[42] D. Krause et al. "Hybrid Parallelization of a Large-Scale Heart Model". In: *Facing the Multicore-Challenge II*. Springer, 2012, pp. 120–132.

[43] S. Krishnamoorthi, M. Sarkar, and W. S. Klug. "Numerical quadrature and operator splitting in finite element methods for cardiac electrophysiology". In: *International Journal for Numerical Methods in Biomedical Engineering* 29 (2003), pp. 1243–1266.

[44] S. Land, S. A. Niederer, and N. P. Smith. "Efficient computational methods for strongly coupled cardiac electromechanics". In: *IEEE transaction on Bio-medical Engineering* 59 (2012), pp. 1219–1228.

[45] *LifeV finite element library*. `https://bitbucket.org/lifev-dev/lifev-release/wiki/Home`.

[46] C. Luo and Y. Rudy. "A dynamic model of the cardiac ventricular action potential. I. Simulations of ionic currents and concentration changes". In: *Circulation Research* 74 (1994), pp. 1071–1096.

[47] C. Luo and Y. Rudy. "A model of the ventricular cardiac action potential. Depolarization, repolarization, and their interaction". In: *Circulation Research* 68 (1991), pp. 1501–1526.

[48] C. J. L. Murray et al. “Global, regional, and national incidence and mortality for hiv, tuberculosis, and malaria during 1990-2013: a systematic analysis for the global burden of disease study 2013”. In: *The Lancet* 384 (2014), pp. 1005–1070.

[49] F. Nobile, A. Quarteroni, and R. Ruiz-Baier. “An active strain electromechanical model for cardiac tissue”. In: *International Journal for Numerical Methods in Biomedical Engineering* 28 (2012), pp. 52–71.

[50] D. A. Nordsletten et al. “Coupling multi-physics models to cardiac mechanics”. In: *Progress in Biophysics and Molecular Biology* 104 (2011), pp. 77–88.

[51] RW Ogden. *Non-linear elastic deformations*. Dover Publications, 1997.

[52] J. H. Omens, K. D. May, and A. D. McCulloch. “Transmural distribution of three-dimensional strain in the isolated arrested canine left ventricle”. In: *The American Journal of Physiology* 261 (1991), pp. 918–928.

[53] A. S. Patelli et al. “Isogeometric approximation of cardiac electrophysiology models on surfaces: an accuracy study with application to the human left atrium”. In: *Computer Methods in Applied Mechanics and Engineering* 317 (2017), pp. 248–273.

[54] P. Pathmanathan et al. “Computational modelling of cardiac electrophysiology: explanation of the variability of results from different numerical solvers”. In: *International Journal for Numerical Methods in Biomedical Engineering* 28 (2012), pp. 890–903.

[55] P. Pathmanathan et al. “The significant effect of the choice of ionic current integration method in cardiac electro-physiological simulations”. In: *International Journal for Numerical Methods in Biomedical Engineering* 27 (2011), pp. 1751–1770.

[56] M. Pennacchio, G. Savaré, and P. Colli Franzone. “Multiscale modeling for the bioelectric activity of the heart”. In: *SIAM Journal on Mathematical Analysis* 37 (2005), pp. 1333–1370.

[57] M. Pfaller et al. “The importance of the pericardium for cardiac biomechanics: from physiology to computational modeling”. In: *Biomechanics and modeling in mechanobiology* 18 (2019), pp. 503–529.

[58] M. Potse et al. “A comparison of monodomain and bidomain reaction-diffusion models for action potential propagation in the human heart”. In: *IEEE Transactions on Biomedical Engineering* 53 (2006), pp. 2425–2435.

[59] M. Potse et al. “Patient-specific modelling of cardiac electrophysiology in heart-failure patients”. In: *Europace: European pacing, arrhythmias, and cardiac electrophysiology: journal of the working groups on cardiac pacing, arrhythmias, and cardiac cellular electrophysiology of the European Society of Cardiology*. 2014.

[60] A. Quarteroni, R. Sacco, and F. Saleri. *Numerical Mathematics*. Springer, 2010.

[61] A. Quarteroni et al. “Integrated heart - coupling multiscale and multiphysics models for the simulation of the cardiac function”. In: *Computer Methods in Applied Mechanics and Engineering* 314 (2017), pp. 345–407.

[62] A. Quarteroni et al. *Mathematical Modelling of the Human Cardiovascular System: Data, Numerical Approximation, Clinical Applications*. Cambridge University Press, 2019.

[63] T. A. Quinn and P. Kohl. “Combining wet and dry research: experience with model development for cardiac mechano-electric structure-function studies”. In: *Cardiovascular Research* 97 (2013), pp. 601–611.

[64] F. Regazzoni, L. Dede’, and A. Quarteroni. “Active contraction of cardiac cells: a model for sarcomere dynamics with cooperative interactions”. In: *Biomechanics and modeling in mechanobiology* 17 (2018), pp. 1663–1686.

[65] D. Romero et al. “Effects of the Purkinje system and cardiac geometry on biventricular pacing: a model study”. In: *Annals of Biomedical Engineering* 38 (2010), pp. 1388–1398.

[66] S. Rossi. “Anisotropic modeling of cardiac mechanical activation”. PhD thesis. EPFL, 2014.

[67] S. Rossi et al. “Orthotropic active strain models for the numerical simulation of cardiac biomechanics”. In: *International journal for numerical methods in biomedical engineering* 28 (2012), pp. 761–788.

[68] S. Rossi et al. “Thermodynamically consistent orthotropic activation model capturing ventricular systolic wall thickening in cardiac electromechanics”. In: *European Journal of Mechanics - A/Solids* 48 (2014), pp. 129–142.

[69] C. F. Royse and A. G. Royse. “The myocardial and vascular effects of bupivacaine, levobupivacaine, and ropivacaine using pressure volume loops”. In: *Anesthesia & Analgesia* 101 (2005), pp. 679–687.

[70] R. Ruiz-Baier et al. “Mathematical modelling of active contraction in isolated cardiomyocytes”. In: *Mathematical Medicine and Biology: a Journal of the IMA* 31 (2014), pp. 259–283.

[71] J. E. Saffitz et al. “Tissue-specific determinants of anisotropic conduction velocity in canine atrial and ventricular myocardium”. In: *Circulation Research* 74 (1994), pp. 1065–1070.

[72] K. Sagawa. “The ventricular pressure-volume diagram revisited”. In: *Circulation Research* 43 (1978), pp. 677–687.

[73] J. Sainte-Marie et al. “Modeling and estimation of the cardiac electromechanical activity”. In: *Computers & Structures* 84 (2006), pp. 1743–1759.

[74] C. Sansour. “On the physical assumptions underlying the volumetric-isochoric split and the case of anisotropy”. In: *European Journal of Mechanics - A/Solids* 27 (2008), pp. 28–39.

[75] A. M. Scher. “The sequence of ventricular excitation”. In: *The American Journal of Cardiology* 14 (1964), pp. 287–293.

[76] P. P. Sengupta et al. “Left Ventricular Structure and Function: basic Science for Cardiac Imaging”. In: *Journal of the American College of Cardiology* 48 (2006), pp. 1988–2001.

[77] J. C. Simo and R. L. Taylor. “Quasi-incompressible finite elasticity in principal stretches. continuum basis and numerical algorithms”. In: *Computer Methods in Applied Mechanics and Engineering* 85 (1991), pp. 273–310.

[78] N. P. Smith et al. “Multiscale computational modelling of the heart”. In: *Acta Numerica* 13 (2004), pp. 371–431.

[79] A. Tagliabue, L. Dede’, and A. Quarteroni. “Complex blood flow patterns in an idealized left ventricle: a numerical study”. In: *Chaos: An Interdisciplinary Journal of Nonlinear Science* 27 (2017), pp. 93939–93964.

[80] A. Tagliabue, L. Dede’, and A. Quarteroni. “Fluid dynamics of an idealized left ventricle: the extended Nitsche’s method for the treatment of heart valves as mixed time varying boundary conditions”. In: *International Journal for Numerical Methods in Fluids* 85 (2017), pp. 135–164.

[81] K. Takizawa, Y. Bazilevs, and T. E. Tezduyar. “Space-time and ALE-VMS techniques for patient-specific cardiovascular fluid-structure interaction modeling”. In: *Mathematical Models and Methods in Applied Sciences* 24 (2014), pp. 2437–2486.

[82] *The Vascular Modeling Toolkit website*. `www.vmtk.org`.

[83] N. A. Trayanova. “Whole-heart modeling applications to cardiac electrophysiology and electromechanics”. In: *Circulation Research* 108 (2011), pp. 113–128.

[84] K. H. ten Tusscher and A. V. Panfilov. “Alternans and spiral breakup in a human ventricular tissue model”. In: *American Journal of Physiology. Heart and Circulatory Physiology* 291 (2006), pp. 1088–1100.

[85] T. P. Usyk, I. J. LeGrice, and A. D. McCulloch. “Computational model of three-dimensional cardiac electromechanics”. In: *Computing and Visualization in Science* 4 (2002), pp. 249–257.

[86] C. Vergara et al. “A coupled 3D-1D numerical monodomain solver for cardiac electrical activation in the myocardium with detailed Purkinje network”. In: *Journal of Computational Physics* 308 (2016), pp. 218–238.

[87] J. G. Wang and G. R. Liu. “A point interpolation meshless method based on radial basis functions”. In: *International Journal for Numerical Methods in Engineering* 54 (2002), pp. 1623–1648.

[88] H. Wendland. “Meshless galerkin methods using radial basis functions”. In: *Mathematics of Computation* 68 (1999), pp. 1521–1531.

[89] N. Westerhof, J. W. Lankhaar, and B. E. Westerhof. “The arterial Windkessel”. In: *Medical & Biological Engineering & Computing* 47 (2009), pp. 131–141.

[90] F. C. Yin, C. C. Chan, and R. M. Judd. “Compressibility of perfused passive myocardium”. In: *American Journal of Physiology. Heart and Circulatory Physiology* 271 (1996), pp. 1864–1870.

[91] O. C. Zienkiewicz and J. Z. Zhu. “The superconvergent patch recovery and a posteriori error estimates. Part 1: The recovery technique”. In: *International Journal for Numerical Methods in Engineering* 33 (1992), pp. 1331–1364.

[92] O. C. Zienkiewicz and J. Z. Zhu. “The superconvergent patch recovery and a posteriori error estimates. Part 2: Error estimates and adaptivity”. In: *International Journal for Numerical Methods in Engineering* 33 (1992), pp. 1365–1382.

MOX Technical Reports, last issues

Dipartimento di Matematica
Politecnico di Milano, Via Bonardi 9 - 20133 Milano (Italy)

34/2019 Antonietti, P. F.; Mazzieri, I.; Melas, L.; Paolucci, R.; Quarteroni, A.; Smerzini, C.; Stupazzini
Three-dimensional physics-based earthquake ground motion simulations for seismic risk assessment in densely populated urban areas

35/2019 Zancanaro, M.; Ballarin, F.; Perotto, S.; Rozza, G.
Hierarchical model reduction techniques for flow modeling in a parametrized setting

33/2019 Regazzoni, F.; Dede', L.; Quarteroni, A.
Machine learning of multiscale active force generation models for the efficient simulation of cardiac electromechanics

32/2019 Fedele, M.
Polygonal surface processing and mesh generation tools for numerical simulations of the complete cardiac function.

31/2019 Pagani, S.; Vitulano, G.; De Blasi, G.; Frontera, A.
High density characterization of the atrial electrical substrate during sinus rhythm in patients with atrial fibrillation

30/2019 Pagani, S.; Manzoni, A.; Quarteroni, A.
Forward uncertainty quantification in cardiac electrophysiology by reduced order modeling and machine learning

29/2019 Dal Santo, N.; Manzoni, A.; Pagani, S.; Quarteroni, A.
Reduced order modeling for applications to the cardiovascular system

28/2019 Infantino, M.; Mazzieri, I.; Ozcebe, A.G.; Paolucci, R.; Stupazzini, M.
Physics-based probabilistic seismic hazard assessment in Istanbul

26/2019 Antonietti, P. F.; Bonaldi, F.; Mazzieri, I.
Simulation of 3D elasto-acoustic wave propagation based on a Discontinuous Galerkin Spectral Element method

27/2019 Tantardini, M.; Ieva, F.; Tajoli, L.; Piccardi, C.
Comparing methods for comparing networks